Department of Precision and Microsystems Engineering

High-resolution RF probing:
Design and Fabrication of a Contactless RF Voltage & Current Probe for Micrometre Resolution Characterisation of Integrated Circuits

Maarten Ivan Henk Jankie

Report no	: 2025.003
Coach	: Dr. T. Hackl
Professor	: Prof. Dr. ir. U. Staufer Prof. Dr. ir. G. Schitter
Specialisation	: Micro & Nano Engineering
Type of report	: Master Thesis
Date	: Friday 3rd January, 2025

TU Delft Delft University of Technology

Challenge the future

High-Resolution RF Probing

Design and Fabrication of a Contactless RF Voltage & Current Probe for Micrometre Resolution Characterisation of Integrated Circuits

by

Maarten Ivan Henk Jankie

to obtain the degree of Master of Science

at the Delft University of Technology,

Student number:	4796861	
Project duration:	September 1, 2023 – January 8, 2025	
Thesis committee:	Prof. Dr. ir. U. Staufer,	TU Delft, (daily) supervisor
	Dr. T. Hackl,	TU Wien, daily supervisor
	Dr. T. Manzaneque Garcia,	TU Delft, committee member
	Prof. Dr. J.F.L. Goosen,	TU Delft, committee member

This thesis is confidential and cannot be made public until December 31, 2025.

An electronic version of this thesis is available at `http://repository.tudelft.nl/`.

TU Delft

Preface

This thesis represents the culmination of a lifetime of learning. I remember always having an aptitude for mathematics and physics, but I was quite late actually realising this. It took a year of studying psychology for me to realise what I actually wanted. I have always been fascinated by the way things work. That is what I loved about my Bachelor in mechanical engineering, directly applying what you learn in the classroom to a real project. This enthusiasm really motivated me to do well and attain as much knowledge as possible, even if it was sometimes a battle.

I have been incredibly fortunate to be surrounded by a supportive network of family and friends who have stood by me through it all. To my girlfriend, Isabelle, and my best friends, Isaac and Sam - you always believed in me, even when I did not, thank you for your unwavering support, I am eternally grateful. I also want to acknowledge Tara, who isn't among us anymore, but will always remain a bright motivation to enjoy and seek out the good times, you will never be forgotten.

This work would not have been possible without the mentorship and collaboration of numerous individuals. I owe special thanks to Urs for our lively discussions and joyful meetings, and to Georg, whose partnership with Urs laid the foundation for this project. Your efforts gave me the opportunity to work with an exceptional team at the ACIN, TU Wien, an amazing experience.

The guidance of my supervisors, Mathias and Thomas, has been instrumental to my success. Mathias, your support during the early stages of this project provided clarity and direction as I navigated the complex world of RF sensing. Although your journey took you beyond academia midway through the project, Thomas stepped in seamlessly, helping me stay on track and ensuring that we reached the finish line. Your insights in design optimization, time performing measurements, and our productive meetings have been invaluable — thank you for your dedication.

Equally vital to this work was the support I received during the fabrication phase. Pieter, Qais, Hande, and Bas, I am deeply grateful for your expertise and guidance in micro- and nano-fabrication techniques. Your expertise and insights helped shape the outcome of this project. I also want to thank the lab technicians who supported me with practical advice and assistance throughout this process.

During my master's program, I was privileged to be a recipient of the ASML scholarship. This experience allowed me to develop skills beyond the academic realm. Marjan, thank you for the opportunities to grow my interpersonal and leadership abilities. To my mentor, Mykyta, your guidance through reflective conversations has been truly transformative. You helped me gain a better understanding of myself, and I often revisited the lessons from our meetings during this journey. One insight that resonates deeply with me is this: "I like to learn by challenging myself". This has been true for this thesis, and I think it will be in the future as well.

Maarten Ivan Henk Jankie
Delft, January 2025

Abstract

In recent years electronics have not only become smaller but also faster. The resulting integrated circuits (IC) often operate at radiofrequencies (RF). As a result of the small distance between features and the high operating frequencies, parasitic coupling can occur between functional elements impacting the functionality of the circuits. Our research therefore presents a novel contactless probe capable of measuring RF voltages and currents with µm-resolution at a bandwidth of 1 to $23\,\mathrm{GHz}$. The probe is fabricated through a multiscale 3D-printing process where the bulk of the chip is printed using Digital Light Processing (DLP) stereolithography. The rest of the probe is printed through a Two-Photon Polymerisation (2PP) process. At the interface, a two-leged cantilever is 2PP printed on top of the DLP print. At the end of the cantilever, a sensing tip is integrated. It contained a triangular loop with a uniform width, and connects the two legs of the cantilever. On top of the triangular loop, a sharp tip is printed. In the last fabrication step, a thin conductive film is deposited by means of thermal evaporation, resulting in a sharp, conductive tip that sits on top of a conductive triangular loop. The loop is connected to the two legs of the cantilever and, hence, a potential over the loop can be measured.

When the probe is brought in proximity to an electrode carrying a time-varying current it inductively couples to the loop. Similarly, when the probe comes close to an electrode subjected to a time-varying voltage, it capacitively couples to the conductive tip. A model-based approach is applied to increase the spatial resolution of the probe. The sharp tip and cantilever allow the probe to be mounted in a modified AFM setup, which is used to accurately position the tip, and determine the tip-circuit distance. The voltage and current are continuously measured while the tip-circuit distance is increased. Sources directly underneath, hence very close to the probe show a non-linear dependence on the tip-circuit distance, whereas parasitic adjacent sources that are further away show an approximately linear dependence on the tip-circuit distance [1]. By fitting the measured data to a mathematical model, the non-linear components can be isolated from the parasitic contributions to the measurement signal. Applying this technique allows us to conduct contactless RF voltage and current measurements with µm-resolution at a bandwidth ranging from 1 to $23\,\mathrm{GHz}$.

References:

[1] M. Poik, T. Hackl, S. Di Martino, B. M. Berger, S. W. Sattler, and G. Schitter, “A contactless method for measuring amplitude and phase of RF voltages up to 26.5GHz,” *IEEE Sensors Journal*, 2024.

Contents

Preface i

Abstract ii

1 Introduction 1

Introduction References 5

2 A 3D-Printed Contactless RF Voltage and Current Probe for Micrometre Resolution Inspection of Integrated Circuits 8
I. Introduction . . . 10
II. Probe Description . . . 11
A. Chip-Body . . . 11
B. Cantilever . . . 12
C. Specialised Tip . . . 12
III. Measurement Setup . . . 13
A. Tip-Circuit Interactions . . . 13
B. Model-Based Measurement Approach . . . 13
IV. Probe Characterisation . . . 14
A. Functional Design Elements . . . 14
B. Inductive Coupling Simulations . . . 14
V. Contactless RF Measurements On A Transmission Line . . . 15
A. Cross-Sectional Measurement . . . 15
B. Stationary Contactless Measurement . . . 15
VI. Conclusion . . . 16
VII. Experimental Section . . . 16
A. Fabrication Process . . . 16
B. Measurement Procedure . . . 17
References . . . 17

3 Skewed Grooves for 3D-Printed Non-Planar Circuits 18
3.1 Literature . . . 18
3.2 Invention Description . . . 19
3.3 Experimental Verification . . . 19
3.4 Considerations . . . 20
3.4.1 Surface Diffusion . . . 20
3.4.2 Self-Capacitance . . . 21
3.4.3 Outgassing . . . 22
3.5 Applications . . . 22

Invention References 23

4 Thesis Conclusion 24

5 Recommendations 26

6 Reflection 28

A A Description Of How One Fabricates A Contactless RF Probe 29
A.1 DLP-Printing . . . 29
A.1.1 Custom Sample Holder . . . 30
A.2 2PP-Printing . . . 32
A.3 Thermal Evaporation . . . 34

A.4 Extra Reference Material 36

B Calculations and models **40**
B.1 Impedance of the loop. 40
B.2 MATLAB code for EMF-simulation 42

1

Introduction

The drive for faster consumer electronics is largely enabled by miniaturisation, resulting in integrated circuits (ICs) that are able to operate in the radiofrequency (RF) bandwidth. These circuits often employ features that are only micrometres in size, or even smaller, with similar separation between them. RF signals passing through these features can induce electromagnetic interference, complicating both the electromagnetic compatibility [1] and circuit characterisation [2]. Conventional contact-based characterisation methods often make use of Ground-Signal-Ground (GSG) probes, as depicted in Figure 1.1. These probes require an ohmic connection with contact pads on the Device Under Test (DUT), to investigate the characteristics of the circuit. These contact pads take up valuable space on the DUT [3]. Nevertheless, GSG probes enable input-output measurements, but require an accurate model of the system between the input and output to attain local information [4]. It therefore still does not poses a method to directly determine local signal properties in between contact pads. Furthermore, the insertion of a probe with low ohmic resistance can influence the measured signal characteristics.

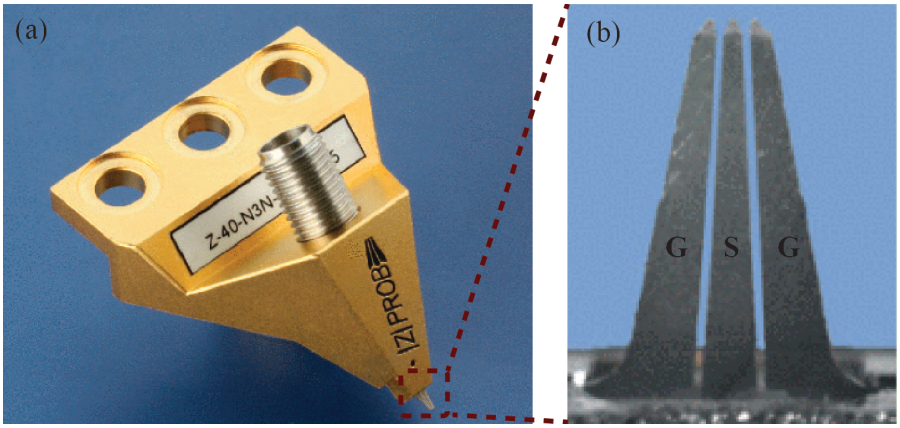

Figure 1.1: an example GSG-probe image a) The first model of the |Z| Probe from SUSS-Rosenberger b) a zoom-in of the probe tip. Adapted from [3]

Built-in RF sensors are also employed to attain localised RF voltage and current measurements. They are integrated into the DUT where they can perform localised measurements [5], [6]. Despite providing localised measurements, these sensors can not be moved around, hence lacking movability. They also occupy valuable chip-area, this is especially the case for sensors that measure both amplitude and phase, such as six-port reflectometers [7]. So, even though contact-based measurement approaches enable measurements with µm-resolution, RFIC designs could greatly benefit from a movable method to directly measure local RF voltages and currents.

Magneto-, and electro-optical probing provide such capabilities. In magneto-optical probes, the characteristics of light is altered when it passes through a material that is influenced by magnetic fields

[8]. Although this technique has been applied for high-frequency characterisation, there are practical complications such as size and movability. Similarly, electro-optical probes make use of electro-optical crystals. Electric fields will be generated in proximity to the DUT as a result of RF voltages. The refractive index of an electro-optical crystal is sensitive to such electric fields [9]. Using a laser the change in refractive index can be measured to determine local RF voltages with a resolution of $8\,\mu\mathrm{m}$ [10]. These probes however include relatively large crystals which can not be moved around obstructions limiting their applicability. Contactless near-field probes overcome this limitation. They make use of capacitive coupling to conduct RF voltage measurements, and inductive coupling to conduct RF current measurements.

Contactless RF voltage probes often consist of an open-ended transmission line, ending in an electrically conductive miniaturised tip [11]–[14]. When such a probing tip is positioned above a circuit element, and perpendicular to the DUT, the probe will capacitively couple to the DUT. The picked-up signal is transmitted to a Vector Network Analyzer (VNA) through an RF transmission line. The signal is then analysed to determine the characteristics of the local RF voltage. This measurement technique does not require ohmic contact, enabling mobile measurements through a passivation layer. With these probes contactless RF voltages up to $8\,\mathrm{GHz}$ with a resolution of $70\,\mu\mathrm{m}$ have been measured [15].

Contactless RF current probes on the other hand employ an electrically conductive loop instead of the tip. One of the loop ends is connected to a ground plane, whereas the other is connected to a VNA. While the probe is kept perpendicular to the DUT, inductive coupling takes place between conductors on the DUT that are parallel to the loop. As a result, a potential difference is generated over the loop which is analysed by the VNA [16], [17]. As with the contactless RF voltage probes, contactless RF current probes are also subjected to capacitive coupling. Ground planes are put in place to shield the sensing loop from these parasitics [17]–[19].

To even further reduce the influence of electric fields, differential field probes have been developed. They feature two loops with an opposite polarity, meaning that the connections to the ground plane, and VNA are switched around for the second loop[20]–[22]. As a result of the capacitive coupling, the signal induced in both loops will have the same polarity. Whereas the potential induced by the inductive coupling will have the opposite polarity. By analysing the difference between these signals, the measurement signal due to inductive coupling can be isolated.

New developments in multi-component probes have resulted in probes capable of simultaneously measuring multiple signals [23]–[27]. They are often configured with a loop with both ends connected to a VNA. By adding the measured signals of both loop ends, the common-mode potential can be found, which is a result of capacitive coupling. It can be analysed to characterise the local RF voltage. Similarly, by subtracting the measured signals from one another, the differential-mode potential can be found, which is a result of inductive coupling. By analyzing the common, and differential-mode potentials the local RF voltage and current can be found.

The spatial resolution, sensitivity, and RF bandwidth are the most important characteristics of contactless RF probes. Design elements often pose trade-offs between these characteristics. Amplifying elements for example increase sensitivity, but only for signals in a specific bandwidth [20], [28]. Miniaturised tips and loops increase the spatial resolution, with a decreased sensitivity as a trade-off [20], [29]. In other methods, several measurements are taken at different separations between the probe and the DUT. It is assumed that the signal sources directly underneath the tip show a strong variation between these separations compared to further away parasitic sources. Therefore by subtracting measurements with different separations between the probe and the DUT, crosstalk from adjacent sample structures can be mitigated for both RF voltage [13], and RF current [18] measurements. The downside of this method is that by subtracting the measurement signals from one another, the sensitivity is decreased.

The reduced sensitivity can be overcome by implementing a model-based measurement approach [30]. A continuous measurement is performed while the tip-circuit distance is increased. Contributions to the measurement signal from local sources directly underneath the tip can be described by a non-linear relation. In contrast, contributions to the measurement signal from adjacent sources, which can be regarded as parasitic cross-talk, can be described by an approximately linear relation. By performing a complex fit to the measurement data, and isolating the non-linear component, local RF voltages can

be characterised without compromising the sensitivity.

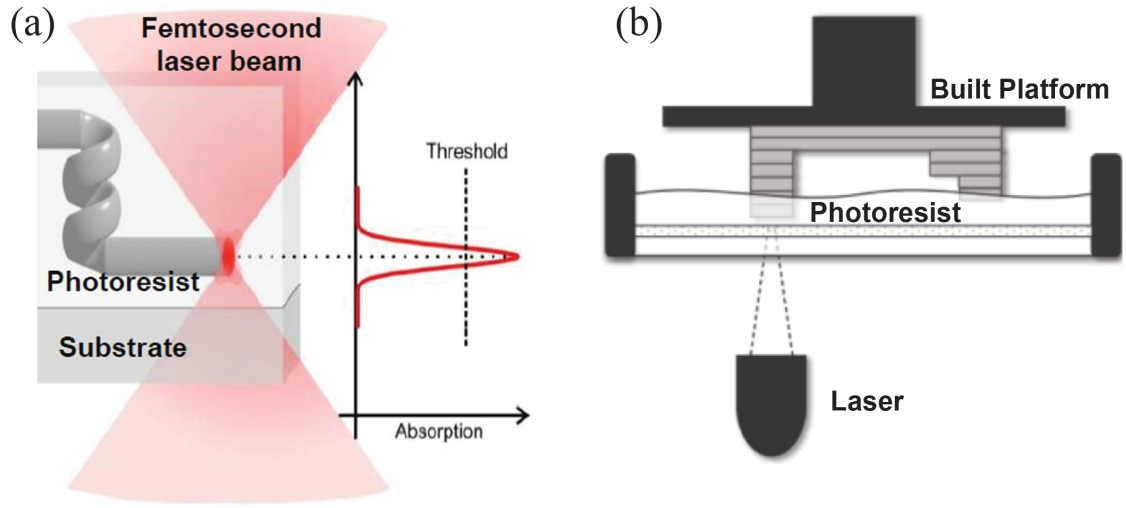

Figure 1.2: A schematic overview of a) Two-Photon Polymerisation 3D-printing, adapted from [31], and b) Digital-Light Processing Stereolithography 3D-printing, adapted from [32].

To accurately determine the tip-circuit distance, the model-based approach employs a modified Atomic Force Microscopy (AFM)-setup, a picture of which can be found in [11]. It requires a probe with a miniaturised tip, suitable for deflection-measurements, like in a conventional AFM-setup [33]. PCB-fabrication techniques that are often utilised for the manufacturing of near-field, or contactless RF current and voltage probes are therefore not suitable. customised hollow AFM cantilevers with specialised tips have been fabricated through multiscale 3D-printing processes [34]–[36]. The chip body is first printed through Digital Light Processing (DLP) stereolithography 3D-printing, a schematic overview of the printing process is depicted in Figure 1.2b. A laser is projected on a polymer bath, after which a photochemical process is set in motion, solidifying a pattern. A stage lifts the substrate after a layer is polymerised, resulting in a three-dimensional structure [37]. This process is suitable for printing parts with $\mu\mathrm{m}$ resolution, with relatively large size, and printing speed, compared to Two-Photon Polymerisation (2PP) 3D-printing. With this technique nm-resolution can be achieved. This resolution is facilitated by the Two-Photon Absorption (2PA) principle. A fs-laser rapidly fires two photons, as depicted in Figure 1.2a. Only in the voxel where the photon intensity is high enough, two photons are simultaneously absorbed through a nonlinear process, inducing a photochemical reaction similar to the one in DLP [31]. To make an electrically conductive, functional device, a metallised layer can be deposited through thermal evaporation. In this process, an electron-beam heats a source material (e.g. a metal) inside of a vacuum chamber, which vaporizes and travels to the substrate where it condenses, forming a thin film [38].

Alternatively, a metal structure can be printed directly through two-photon photoreduction. This technique is similar to 2PP, as it also relies on 2PA. By using a different ink in the process, 2PA will induce a reduction of metallic ions, instead of inducing a polymerisation reaction [31], [39]–[41]. These inks are however not commercially available, increasing the risk of compromising the valuable 2PP setup with a custom ink. Transfer lift-off patterning could also be applied to attain non-planar electrically conductive structures [42]. A structure is first patterned in a lithography step. A thin film is subsequentially deposited (i.e. through thermal evaporation) on the patterned, and unpatterned areas. The pattern is then lifted off the substrate including the thin film, leaving behind the thin film that is deposited directly on the substrate. It can now be transferred to other substrates by pressing them together. This process has many steps and lacks reliability and repeatability.

Stationary shadow mask evaporation is a technique that can be combined with 3D-printing to create metalised patterns. It was mentioned before that in a thermal evaporation process material is vaporized and travels to a substrate where it condenses to form a thin film. The material vapour travels in an approximately straight line and can be blocked with a mask [43]. By integrating the mask into a 3D-

printed structure a repeatable fabrication process can be created.

This research aims to create a novel multi-component probe by combining a multiscale 3D-printing process with a stationary shadow mask evaporation process. The resulting probe will be suitable for deflection-measurements, like in a conventional AFM-setup. It will hence also be suitable for performing measurements according to the model-based approach as presented in [30]. The research question posed in this research is therefore formulated as follows:

> **"Can an exchangable probe conduct contactless radio-frequency voltage, and current measurements at a bandwidth of 1 to $26.5\,\mathrm{GHz}$ with micrometre-resolution?"**

The report features a research paper in chapter 2, which presents the characteristics, and fabrication process of the probe. To realise the probe, a novel fabrication technique has been invented to create mutually isolated signal traces by means of 3D-printing in combination with Physical Vapor Deposition (PVD), which is presented in chapter 3. The conclusions of the thesis have been collected in chapter 4. In chapter 5, recommendations are given for further research. A reflection on the whole process is given in chapter 6. Detailed information on the fabrication process is presented in Appendix A. Lastly, the calculations and a `MATLAB`-model is provided in Appendix B. The only thing that remains is to wish you an enjoyable and insightful read.

Introduction References

[1] Y.-C. Chang, P.-Y. Wang, D.-C. Chang, and S.-S. Hsu, "A low-loss fully integrated cmos active probe for gigahertz conducted emi test," *IEEE Transactions on Microwave Theory and Techniques*, vol. 67, no. 4, pp. 1652–1660, Apr. 2019.

[2] M. Poik, T. Hackl, S. Di Martino, M. Schober, J. Dang, and G. Schitter, "Analysis of cross-talk induced measurement errors in model-based rf voltage sensing," in *2023 IEEE International Instrumentation and Measurement Technology Conference (I2MTC)*, 2023, pp. 1–6.

[3] A. Rumiantsev and R. Doerner, "Rf probe technology: History and selected topics," *IEEE Microwave Magazine*, vol. 14, no. 7, pp. 46–58, 2013.

[4] V. Solomko, O. Özdamar, R. Weigel, and A. Hagelauer, "Model of substrate capacitance of mosfet rf switch inspired by inverted microstrip line," in *51st IEEE European Solid-State Device Research Conference (ESSDERC)*, Grenoble, France: IEEE, Sep. 2021, pp. 207–210.

[5] S. Ziegler, R. C. Woodward, H. H.-C. Iu, and L. J. Borle, "Current sensing techniques: A review," *IEEE Sensors Journal*, vol. 9, no. 4, pp. 354–376, Apr. 2009.

[6] O. Özdamar, A. M. Hagelauer, R. Weigel, and V. Solomko, "An rf voltage detector with low harmonic feedback for antenna tuning switches," in *2019 IEEE International Conference on Microwaves, Antennas, Communications and Electronic Systems (COMCAS)*, Tel-Aviv, Israel: IEEE, 2019, pp. 1–5.

[7] R. G. Venter, R. Hou, K. Buisman, M. Spirito, K. Werner, and L. C. N. de Vreede, "A package-integratable six-port reflectometer for power devices," in *2014 IEEE MTT-S International Microwave Symposium (IMS)*, IEEE, 2014, pp. 1–4.

[8] G. Chen, Z. Jin, and J. Chen, "A review: Magneto-optical sensor based on magnetostrictive materials and magneto-optical material," *Sensors and Actuators Reports*, vol. 5, p. 100 152, Jun. 2023.

[9] D.-J. Lee, N.-W. Kang, J.-H. Choi, J. Kim, and J. F. Whitaker, "Recent advances in the design of electro-optic sensors for minimally destructive microwave field probing," *Sensors*, vol. 11, no. 1, pp. 806–824, 2011.

[10] J. Urbonas, K. Kim, and P. H. Aaen, "Direct e-field measurement and imaging of oscillations within power amplifiers," *IEEE Transactions on Instrumentation and Measurement*, vol. 68, no. 8, pp. 2971–2978, Aug. 2019.

[11] M. Poik, T. Hackl, S. Di Martino, B. M. Berger, S. W. Sattler, and G. Schitter, "A contactless method for measuring amplitude and phase of rf voltages up to 26.5ghz," *IEEE Sensors Journal*, 2024.

[12] W. Fang, H. Qiu, C. Luo, L. Wang, and E. Shao, "Noncontact rf voltage sensing of a printed trace via a capacitive-coupled probe," *IEEE Sensors Journal*, vol. 18, no. 21, pp. 8873–8882, Nov. 2018.

[13] R. Kantor and I. V. Shvets, "Measurement of electric-field intensities using scanning near-field microwave microscopy," *IEEE Transactions on Microwave Theory and Techniques*, vol. 51, no. 11, pp. 2228–2234, Nov. 2003.

[14] N. Dehghan and S. C. Cripps, "A novel in-situ calibration technique for a high resolution e-field probe," in *2015 IEEE MTT-S International Microwave Symposium (IMS)*, Phoenix, AZ, USA: IEEE, Mar. 2015, pp. 1–3.

[15] R. Hou, M. Spirito, R. Heeres, F. van Rijs, and L. C. N. de Vreede, "Non-intrusive near-field characterization of distributed effects in large-periphery ldmos rf power transistors," in *2015 IEEE MTT-S International Microwave Symposium (IMS)*, IEEE, 2015, pp. 1–3.

[16] H. Qiu, W. Fang, Y. En, *et al.*, "Movable noncontact rf current measurement on a pcb trace," *IEEE Transactions on Instrumentation and Measurement*, vol. 66, no. 9, pp. 2464–2473, Sep. 2017.

[17] N. Ando, N. Masuda, N. Tamaki, *et al.*, "Miniaturized thin-film magnetic field probe with high spatial resolution for lsi chip measurement," New Industry Creation Hatchery Center (NICHe), Tohoku University, Tech. Rep., 2004.

[18] Y. T. Chou and H. C. Lu, "Space difference magnetic near-field probe with spatial resolution improvement," *IEEE Transactions on Microwave Theory and Techniques*, vol. 61, no. 12, pp. 4233–4244, Dec. 2013.

[19] Z. Yan, W. Liu, J. Wang, D. Su, X. Yan, and J. Fan, "Noncontact wideband current probes with high sensitivity and spatial resolution for noise location on pcb," *IEEE Transactions on Instrumentation and Measurement*, vol. 67, no. 12, pp. 2881–2891, Dec. 2018.

[20] J. Wang, Z. Yan, J. Liu, Y. Zhou, C. Fu, and D. Su, "Miniature active differential magnetic field probe with high sensitivity for near-field measurements," *IEEE Transactions on Antennas and Propagation*, vol. 70, no. 2, pp. 1575–1580, Feb. 2022.

[21] W. Shao, Y. Chen, L. Huang, and W. Fang, "An asymmetric correction method for differential double-loop magnetic field probing system," *IEEE Transactions on Antennas and Propagation*, vol. 71, no. 10, pp. 6349–6354, 2023.

[22] G. Li, W. Shao, R. Chen, Y. Zhang, and Z. Wang, "Ultrawideband differential magnetic near field probe with high electric field suppression," *IEEE Sensors Journal*, vol. 20, no. 14, pp. 7669–7676, Jul. 2020.

[23] R. Yang, X.-C. Wei, Y.-F. Shu, D. Yi, and Y.-B. Yang, "A miniature multi-component probe for near-field scanning," *IEEE Transactions on Antennas and Propagation*, vol. 67, no. 11, pp. 6821–6828, Nov. 2019.

[24] L. Wang, X. Liu, W. Shao, and Z. Zhu, "An ultrawideband four-port composite probe with simultaneous measurement of multicomponent fields and improvement of electric-field suppression," *IEEE Transactions on Components, Packaging and Manufacturing Technology*, vol. 13, no. 8, pp. 1278–1286, Aug. 2023.

[25] W. Shao, W. Fang, Y. Huang, Z. Liu, and X. Dong, "Simultaneous measurement of electric and magnetic fields with a dual probe for efficient near-field scanning," *IEEE Transactions on Antennas and Propagation*, vol. 67, no. 4, pp. 2859–2864, Apr. 2019.

[26] C. Luo, W. Fang, Y. Shen, H. Qiu, F. Yu, and H. Li, "Collocated and simultaneous measurements of rf current and voltage on a trace in a noncontact manner," *IEEE Transactions on Microwave Theory and Techniques*, vol. 67, no. 6, pp. 2406–2415, Jun. 2019.

[27] W. Shao, Z. Yi, X. He, W. Fang, C. Zhou, and J. Liu, "Novel calibration method for the asymmetric probing in the near-field measurement with a dual probe," *IEEE Transactions on Microwave Theory and Techniques*, vol. 69, no. 12, pp. 5439–5448, Dec. 2021.

[28] W. Shao, J. Li, Q. Huang, E. Shao, and J. Liu, "A two-turn loop active magnetic field probe design for high sensitivity near-field measurement," *IET Science, Measurement & Technology*, vol. 16, no. 1, pp. 40–49, Jan. 2022.

[29] L. Fumagalli, G. Ferrari, M. Sampietro, *et al.*, "Nanoscale capacitance imaging with attofarad resolution using ac current sensing atomic force microscopy," *Nanotechnology*, vol. 17, no. 18, pp. 4581–4587, Sep. 2006.

[30] M. Poik, T. Hackl, S. D. Martino, M. Schober, J. Dang, and G. Schitter, "Model-based rf sensing for contactless high-resolution voltage measurements," *IEEE Transactions on Instrumentation and Measurement*, vol. 72, pp. 1–8, 2023.

[31] V. Harinarayana and Y. C. Shin, "Two-photon lithography for three-dimensional fabrication in micro/nanoscale regime: A comprehensive review," *Optics & Laser Technology*, vol. 142, p. 107 180, Oct. 2021.

[32] E. M. Maines, M. K. Porwal, C. J. Ellison, and T. M. Reineke, "Sustainable advances in sla/dlp 3d printing materials and processes," *Green Chemistry*, vol. 23, no. 18, pp. 6863–6897, Sep. 2021.

[33] O. H. Olubowale, S. Biswas, G. Azom, *et al.*, ""may the force be with you!" force-volume mapping with atomic force microscopy," *ACS Omega*, vol. 6, no. 40, pp. 25 860–25 875, 2021.

[34] M. Blankespoor, T. Manzaneque, and M. K. Ghatkesar, “Discrete femtolitre pipetting with 3d printed axisymmetrical phaseguides,” *Small Methods*, vol. 8, no. 3, p. 2 300 942, Mar. 2024.

[35] R. C. Kramer, E. J. Verlinden, L. Angeloni, *et al.*, “Multiscale 3d-printing of microfluidic afm cantilevers,” *Lab on a Chip*, vol. 20, no. 2, pp. 311–319, Jan. 2020.

[36] P. F. J. van Altena, “Multiscale 3d printed polymer probes for single cell experiments,” M.S. thesis, TU Delft, 2021.

[37] A. Kafle, E. Luis, R. Silwal, H. M. Pan, P. L. Shrestha, and A. K. Bastola, “3d/4d printing of polymers: Fused deposition modelling (fdm), selective laser sintering (sls), and stereolithography (sla),” *Polymers*, vol. 13, no. 18, p. 3101, 2021.

[38] M. Luitz, M. Lunzer, A. Goralczyk, *et al.*, “High resolution patterning of an organic–inorganic photoresin for the fabrication of platinum microstructures,” *Advanced Materials*, vol. 33, no. 37, p. 2 101 992, 2021.

[39] J. Choi, H. Kim, and S. K. Saha, “Rapid printing of metal nanostructures through projection-based two-photon reduction,” *Manufacturing Letters*, vol. 36, no. C, pp. 1–4, 2023.

[40] S. Tabrizi, Y. Cao, H. Lin, and B. Jia, “Two-photon reduction: A cost-effective method for fabrication of functional metallic nanostructures,” *Science China: Physics, Mechanics and Astronomy*, vol. 60, no. 3, p. 034 201, Mar. 2017.

[41] Y.-Y. Cao, N. Takeyasu, T. Tanaka, X.-M. Duan, and S. Kawata, “3d metallic nanostructure fabrication by surfactant-assisted multiphoton-induced reduction,” *Small*, vol. 5, no. 10, pp. 1144–1148, Mar. 2009.

[42] E. J. Smythe, M. D. Dickey, G. M. Whitesides, and F. Capasso, “A technique to transfer metallic nanoscale patterns to small and non-planar surfaces,” *ACS Nano*, vol. 3, no. 1, pp. 59–65, 2009.

[43] T. Schallenberg, C. Schumacher, S. Gundel, and W. Faschinger, “Shadow mask technology,” *Thin Solid Films*, vol. 412, no. 1-2, pp. 24–29, Jun. 2002.

2

A 3D-Printed Contactless RF Voltage and Current Probe for Micrometre Resolution Inspection of Integrated Circuits

A 3D-Printed Contactless RF Voltage and Current Probe for Micrometre Resolution Inspection of Integrated Circuits

Maarten Jankie, Thomas Hackl, Urs Staufer, Georg Schitter

***Abstract*—As a result of current trends in miniaturisation and the need for faster circuits, integrated circuit (IC) design has become more complex. Closely packed conductors carrying radiofrequency (RF) signals are subjected to parasitic coupling, complicating the IC design and validation. Contact probes have been developed to make an ohmic connection and characterise ICs. These require contact pads on the IC, taking up valuable space. Alternatively, near-field probing techniques, that utilize capacitive and inductive coupling, have been employed for local RF voltage and current characterisation. In this research, a near-field probe is developed through a multiscale 3D-printing process. It contains a miniaturised conductive loop, enclosing an area of $12.5\,\mu\mathrm{m}^2$, and a conductive tip with an apex radius of $100\,\mathrm{nm}$. A model-based approach, that makes use of the discrepancy between parasitic long-range, and local short-range contributions to the measurement signal, is expanded to conduct both RF voltage and current measurements with increased spatial resolution. With this approach, contactless RF voltage measurements are performed through capacitive coupling with $8\,\mu\mathrm{m}$ resolution, while the spatial resolution for inductively coupled current probing is simulated to be $3.11\,\mu\mathrm{m}$. The achieved measurement bandwidth ranges from 1 to $23\,\mathrm{GHz}$.**

***Index Terms*—Contactless Model-Based RF Probing, Multi-component Probe, Miniaturised loop, Multiscale 3D printing.**

I. Introduction

THE drive for faster devices has led to the rise of Radiofrequency Integrated Circuits (RFICs), which pose challenges in electromagnetic compatibility [1] as well as characterisation [2]. Conventional contact-based characterisation methods use radiofrequency (RF) contact probes, which require contact pads to connect to the Device Under Test (DUT) [3]. In the case of RFICs, features are often small compared to the contact pads, making it difficult to characterise local voltages and currents with μm-resolution. Parasitic coupling to surrounding features further complicates the local identification of voltages and currents, as contact measurements require a well-defined model between the measurement input and output [4]. Alternatively, built-in RF sensors can be integrated into the device to acquire local RF voltage and current measurements [5], [6]. These however take up space on the chip and can only perform measurements in one location. So even though contact-based measurement techniques allow for global circuit characterisation, a method for conducting movable local RF voltage and current measurements with μm-resolution could greatly benefit the development of new RFICs.

Contactless probing techniques have been developed to measure local RF voltages. These probes often consist of an open-ended RF transmission line that ends in a sharp tip [7]–[11]. The tip is positioned above and perpendicular to the DUT during a measurement. The tip picks up an RF voltage through capacitive coupling. The resulting signal is transmitted to a Vector Network Analyzer (VNA) where its properties are measured.

Similarly, local RF currents can be measured using contactless current probes [12]–[15]. These probes feature an electrically conductive loop with one end connected to a signal trace and the other to a ground plane. During a measurement, the loop is positioned above and parallel to a transmission line on the DUT. A potential in the loop is generated through inductive coupling between the loop and DUT. The generated signal is transmitted to a VNA where it is analysed to characterise local RF current distributions in the DUT. These probes are subjected to parasitic capacitive coupling between the conductive loop and DUT. Shielding ground planes are employed to minimise the influence of these parasitics [12], [13], [15].

This limitation can be overcome with differential field probes. These make use of two parallel loops with opposite polarities [16]–[18]. The potential induced as a result of the current has an opposing polarity in both loops, whereas the potential induced by the voltage has a matching polarity. By analysing the potential difference between both loops local RF currents can accurately be characterised.

Recently multi-component probes have been developed, capable of simultaneously measuring multiple signals [19]–[23]. Probes that allow for simultaneous RF voltage and current measurements often consist of two open-ended transmission lines that are connected through a conductive loop. During a measurement, the loop is positioned above and parallel to a transmission line on the DUT. A potential is induced in the loop, and transmitted through the RF transmission lines to a VNA. These are added to get the common-mode potential, which is used to characterise local RF voltages. Local RF currents can similarly be characterised by subtracting the measured signals from one another, to find the differential-mode potential.

Contactless probes are evaluated based on spatial resolution, sensitivity, and RF bandwidth. Designs often make trade-

M. Jankie and U. Staufer are with the department of Precision and Microsystems Engineering (PME), TU Delft, Mekelweg 2, 2628CD Delft, The Netherlands

T. Hackl and G. Schitter are with the Automation and Control Institute (ACIN), TU Wien, Gusshausstrasse 27-29, 1040 Vienna, Austria

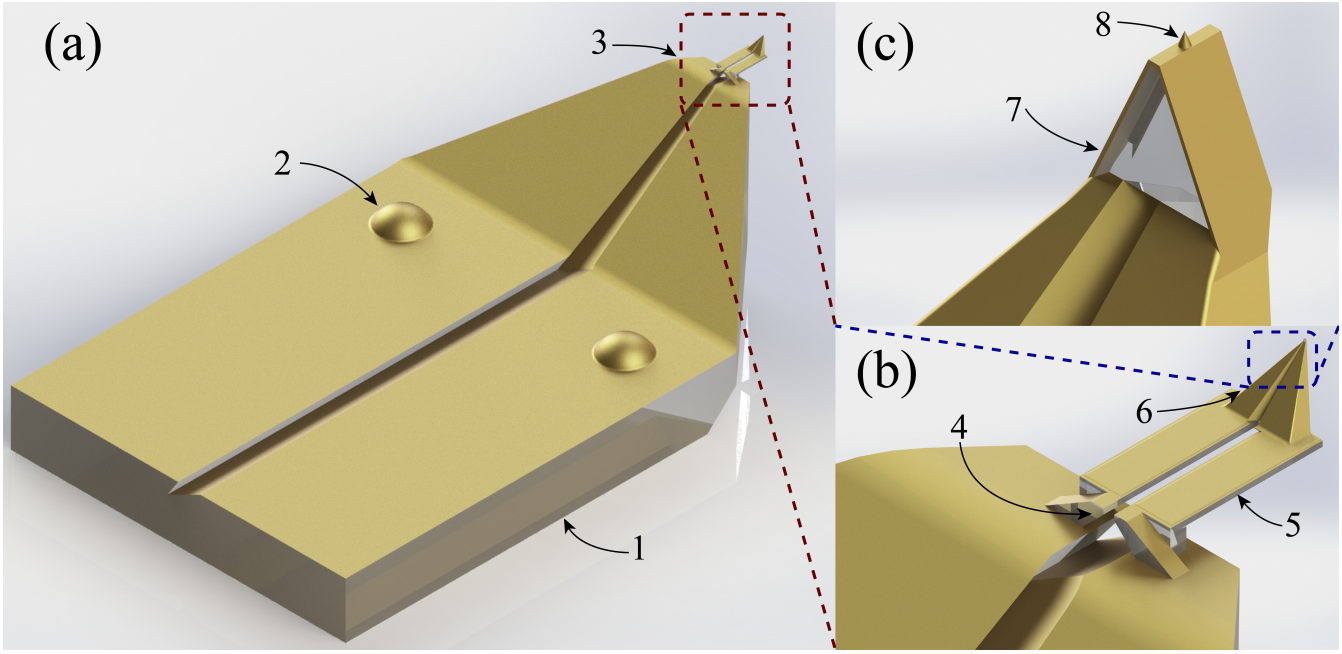

Fig. 2.1. Renders of the probe design with a) an overview of the chip-body (1), showing the alignment hemispheres (2), and the build-pedestal (3). b) shows a zoom-in of the 2PP printed structure consisting of a base (4), two-legged cantilever (5) and sensing tip (6). c) shows a zoom-in on the sensing part of the tip, consisting of a conductive triangular loop (7) with a sharp conductive tip (8) on top.

offs between these characteristics. Amplifying elements for example increase sensitivity, but decrease bandwidth since they only amplify signals in specific bandwidths [16], [24]. Similarly, miniaturised loops and tips inherently increase the spatial resolution, but decrease the sensitivity [16].

The spatial resolution can be increased by taking several measurements at different separations between the probe and the DUT. In this method, measurements are taken at various heights and are subtracted from one another, to mitigate crosstalk of adjacent sample structures. This approach has been applied to both, RF voltage [9] and current [12] measurements. As the increments between measurements get smaller, the resolution improves, while the sensitivity decreases. To overcome this, a model-based approach has been developed [25]. Here the distance between the tip and DUT is continuously varied during a measurement. Voltage sources directly underneath the tip will show non-linear capacitive coupling, whereas adjacent voltage sources will lead to linear capacitive coupling. By isolating the non-linear terms in the fitted model, the voltage distribution caused by voltage sources directly underneath the tip can be characterised, with µm-resolution.

This paper presents a novel multi-component probe capable of simultaneous local RF voltage and current measurements. It is fabricated through a multiscale 3D-printing process, followed by a thin film deposition step. The design includes a two-legged cantilever ending in a sharp sensing tip, enabling precise tip-circuit positioning as in a standard Atomic Force Microscopy (AFM)-setup [26]. The design is hence, suitable for conducting contactless RF measurements according to the model-based approach, presented in [25]. The model has been expanded to conduct not only contactless RF voltage measurements but also current measurements.

The paper presents the probe design in Section II, followed by a description and model of the measurement setup in Section III. The geometries of the fabricated probes are characterised in Section IV. In Section V, contactless RF measurements are performed on a microstrip. The conclusions of the research are presented in Section VI. Lastly, the fabrication process and measurement procedure is described in Section VII.

II. Probe Description

An overview of the probe geometry is shown in Fig. 2.1. The probe is fabricated through a multiscale 3D-printing process similar to the ones described in [27]–[29], followed by a thin film deposition step, a detailed description of the fabrication process is provided in Section VII. A chip-body, functioning as the interface between the probe and measurement setup, is first printed by means of Digital Light Processing (DLP) stereolithography. Directly on top of the chip-body, the cantilever and specialised tip are printed through Two-Photon Polymerisation (2PP). To facilitate an electrical connection, an electrically conductive thin film is deposited on top of the probe through a thermal evaporation process. To interface with the measurement setup, the probe is glued to a Printed Circuit Board (PCB) as depicted in Fig. 2.2c. The PCB contains two SMA connectors that transmit the measured RF signals to a VNA, where both signals are analysed to locally characterise RF voltages and currents.

A. Chip-Body

The chip-body, depicted in Fig. 2.1a, functions as a mechanical and electrical interface between the PCB and the probe. It

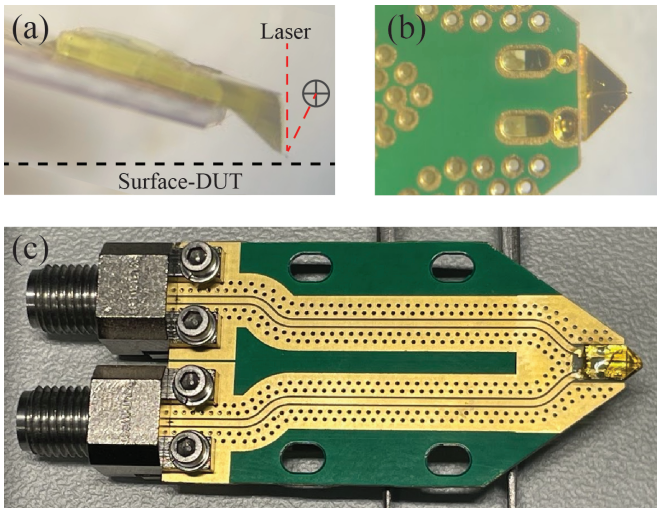

Fig. 2.2. Overview of a probe mounted on a PCB. a) shows the angle of incidence with the surface of the DUT. b) Backside of the PCB zoomed in on the alignment holes. c) overview of the probe-PCB assembly showing connection from the probe to the transmission lines and SMA connectors.

features two hemispheres that aid in aligning the probe to the PCB. To account for tolerances in the fabrication processes, the PCB includes a via hole and via slot, where the hemispheres are seated during glueing as depicted in Fig. 2.2b. The chip-body contains two signal paths that end in two contact pads (c.f. Fig. 2.1a), which were realised through the integration of a separation along the middle, the design of which is discussed in Chapter 3. When the probe is glued to the PCB, the contact pads on the chip-body are pressed to the contact pads on the PCB, facilitating an electrical interface between the two.

The design freedom offered by the 3D-printing process is utilized to integrate additional functionalities into the design of the chip-body. As such, the height of the probe is increased to accommodate handling and positioning with tweezers. Furthermore, a slope is included that compensates for the thickness of the PCB. It can be seen from Fig. 2.2a that the probe needs to extend a certain amount to come in proximity to the DUT. By integrating a sloped extension, the probe can reach beyond the PCB. the slope features two signal paths that extend from the contact pads.

A build-pedestal for multiscale 3D-printing can be found at the top of the slope. It features the same two mutually isolated signal paths that are continued along the entire chip-body. The build-pedestal has distinct features, such as shape, and separation between the signal paths, that function as alignment markers during the subsequent 2PP steps. It can be seen from Fig. 2.2a that when the probe is mounted in the measurement setup, features extending past the build-pedestal still have a line of sight from above, which is a requirement for the laser reflection onto the photodiode.

B. Cantilever

The design includes a two-legged cantilever as depicted in Fig. 2.1b. It features a base, which is printed directly on top of the build-pedestal, and forms a foundation for the 2PP printed part of the probe. A slope is included in the base to create a signal path from the chip-body, to the two-legged cantilever. It includes two wide pillars that support the cantilever.

The two signal paths from the base are continued on the two-legged cantilever, leading to the sensing tip. As the cantilever extends beyond the chip-body, a laser is reflected of the backside, enabling deflection-measurements, like in a standard AFM-setup [26]. To prevent the cantilever from sagging during fabrication, it is printed at an angle of $45°$, with small increments of $8\,\mu\mathrm{m}$ that have an overlapping length of $4\,\mu\mathrm{m}$. To reduce the roughness caused by the increments, a $1\,\mu\mathrm{m}$ thin layer was printed on top of the cantilever, improving the laser reflection, and signal transmission.

The two legs of the cantilever come together at the end in a square structure. This structure forms the base for the tip. The tip contains two signal paths, hence, electrical isolation between the signal paths is maintained, while the base provides mechanical stability to the tip during the subsequent fabrication steps.

C. Specialised Tip

The tip is formed by a forward-angled square pyramid, easing the optical positioning of the tip apex during measurement. It is printed to a height of $100\,\mu\mathrm{m}$ so that it can be easily manoeuvred around obstructions, such as bonding wires. It contains a separation along the middle similar to the one applied to the chip-body, to create two mutually isolated signal paths, which will be discussed in Chapter 3.

A miniaturised triangular loop is situated on top of the tip, as depicted in Fig. 2.1c. It is made electrically conductive through a thermal evaporation process, and connects the two signal paths coming from the cantilever. Small overhangs are put in place to prevent thin film deposition on the sidewalls of the loop. The structure has a constant width of $2\,\mu\mathrm{m}$. As depicted in Fig. 2.5, both the base and height of the triangular structure are $5\,\mu\mathrm{m}$ long. Currents in the DUT that produce a time-varying electromagnetic flux will induce a potential over the loop, which can be analysed with the VNA to localy determine the phase and magnitude of the current.

A small plane as depicted in 2.1c. is situated at the apex of the triangular loop. A small cone is printed on top of this plane, using the maximum achievable resolution with the setup. The resulting structure as seen in Fig. 2.4, has an apex radius of approximately $100\,\mathrm{nm}$. It acts as an open-ended transmission line, that picks up time-varying electric fields, generated by time-varying voltages. At the same time, it acts as the apex of the tip in AFM measurements.

The probe design features a separate loop and tip structure. This allows for independent iteration of the functional design elements. This does however pose a trade-off. The small plane on which the conic tip is situated, acts as a parallel plate capacitor. This introduces noise during contactless voltage measurements, deteriorating the spatial resolution. The height of the conic tip can be increased to mediate the influence of the parallel plate capacitor. This however increases the distance between the loop to the DUT resulting in a lower sensitivity during current measurements.

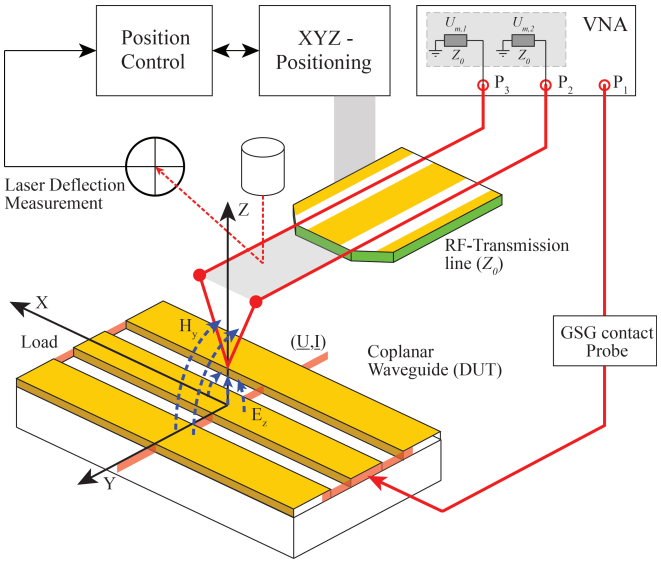

Fig. 2.3. Schematic overview of RF measurement setup. adapted from [7]

III. Measurement Setup

The experimental setup is depicted in Fig. 2.3, a picture of which can be found in [7]. The probe is glued to a PCB containing two RF transmission lines with a similar characteristic impedance (Z_0) of $50\,\Omega$. The PCB-probe assembly is mounted in the modified AFM-setup, enabling the probe to be positioned above the DUT with nm-accuracy. The two signal paths originating from the PCB-probe assembly are connected to the VNA with the SMA connectors depicted in Fig. 2.2c. An RF signal is delivered to the DUT through a Ground-Signal-Ground (GSG) contact probe.

A. Tip-Circuit Interactions

The inductive and capacitive coupling effects can be analysed individually to locally determine the RF voltage-, and current. The local RF voltage $\underline{U}$ induces a common-mode potential $\sum \underline{U}_\mathrm{m} = \underline{U}_\mathrm{m,2} + \underline{U}_\mathrm{m,3}$, whereas the local RF current $\underline{I}$ is picked-up as a differential-mode potential $\Delta\underline{U}_\mathrm{m} = \underline{U}_\mathrm{m,2} - \underline{U}_\mathrm{m,3}$. The capacitive coupling can be modelled as the tip-circuit capacitance C in series with two parallel transmission lines. Whereas the inductive coupling is modelled as the tip-circuit inductance L, in series with the loop, which in turn is in series with two parallel transmission lines. The resulting relations are described by the equations below [7]:

$$\sum \underline{U}_\mathrm{m} = \underline{U} \cdot \frac{j\omega 2 Z_0 C}{2 + j\omega Z_0 C} \approx \underline{U} \cdot j\omega Z_0 C \tag{2.1}$$

$$\Delta\underline{U}_\mathrm{m} = \underline{I} \cdot \frac{j\omega 2 Z_0 L}{2Z_0 + Z_l} \approx \underline{I} \cdot j\omega L \tag{2.2}$$

The simplifications made in equations (2.1) & (2.2) are only valid as long as $C \ll \frac{2}{\omega Z_0}$ and $Z_l \ll 2Z_0$. Where the variables ω, Z_l, and $Z_0 = 50\,\Omega$ denote the angular frequency, the impedance of the loop, and the impedance of the transmission lines respectively. These assumptions hold for frequencies $\omega < 26\,\mathrm{GHz}$, and the proposed probe geometry and setup.

B. Model-Based Measurement Approach

The model-based approach as presented in [7], provides a method to eliminate parasitic cross-talk by performing continuous voltage measurements while varying the tip-circuit distance. The total capacitance C [30] and inductance L between the probe and the circuit, are both dependent on the tip-circuit distance z. They can be subdivided in short-range nonlinear components that originate from electrodes right underneath the tip, and long-range approximately linear components that are due to parasitic sources originating further away from the tip. The following equations mathematically depict these effects:

$$C(z) = \underbrace{C_\mathrm{nl}(z)}_{\text{short-range}} + \underbrace{C_\mathrm{lin}(z)}_{\text{long-range}} \tag{2.3}$$

$$L(z) = \underbrace{L_\mathrm{nl}(z)}_{\text{short-range}} + \underbrace{L_\mathrm{lin}(z)}_{\text{long-range}} \tag{2.4}$$

The nonlinear component of the capacitance $C_\mathrm{nl}(z)$ can be described by a logarithmic dependency on the tip-circuit distance [7], [30]. Similarly, the inductance $L_\mathrm{nl}(z)$ follows an inverse dependence on the tip-circuit distance. These relations are described by the following equations:

$$C_\mathrm{nl}(z) = C_0 \cdot \ln\left(1 + \frac{R_\mathrm{eff}}{z}\right) \tag{2.5}$$

$$L_\mathrm{nl}(z) = L_0 \cdot \left(1 + \frac{A_\mathrm{eff}}{z}\right) \tag{2.6}$$

Where C_0 and L_0 represent a constant capacitance, and inductance. The terms R_eff and A_eff denote the effective tip-apex radius and the effective area enclosed by the loop, which account for the shape and size of the tip. It is evident from Equations (2.5) & (2.6) that especially for small tip-circuit distances z, on the order of R_eff and A_eff, the non-linear components become significant. Parasitic coupling between the probe and circuit parts at larger distances, however, follow linear dependencies, described by $C_\mathrm{lin} = a \cdot z + b$, and $L_\mathrm{lin} = c \cdot z + d$. As such, the signals measured by the VNA according to equations (2.1) & (2.2), can also be subdivided into a long-, and short-range component.

$$\sum \underline{U}_\mathrm{m}(z) \propto \underbrace{\underline{U} \cdot C_\mathrm{nl}(z)}_{\text{short-range}} + \underbrace{\underline{U}_\mathrm{lin} \cdot C_\mathrm{lin}(z)}_{\text{long-range}} \tag{2.7}$$

$$\Delta\underline{U}_\mathrm{m}(z) \propto \underbrace{\underline{I} \cdot L_\mathrm{nl}(z)}_{\text{short-range}} + \underbrace{\underline{I}_\mathrm{lin} \cdot L_\mathrm{lin}(z)}_{\text{long-range}} \tag{2.8}$$

The local short-range coupling terms are represented by $C_\mathrm{nl}(z)$, and $L_\mathrm{nl}(z)$. Looking back at equations (2.5) & (2.6), it is presumed that the non-linear coupling terms are significant only for circuit parts close to the tip. Hence, the non-linear coupling terms correspond only to local RF voltages $\underline{U}$ [7] and currents $\underline{I}$. The remaining parasitic coupling effects between circuit elements and the probe follow a linear dependency on the tip-circuit distance, and are therefore all represented into a combined long-range voltage $\underline{U}_\mathrm{lin}$ [7] and current $\underline{I}_\mathrm{lin}$.

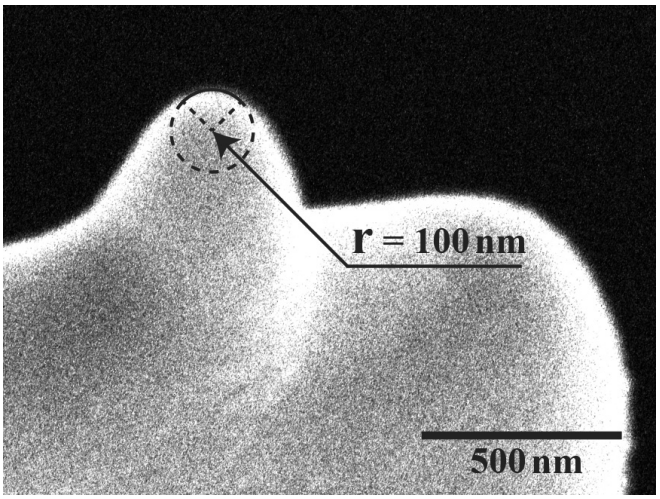

Fig. 2.4. SEM image of the electrically-conductive miniaturised tip showing the apex radius of the tip.

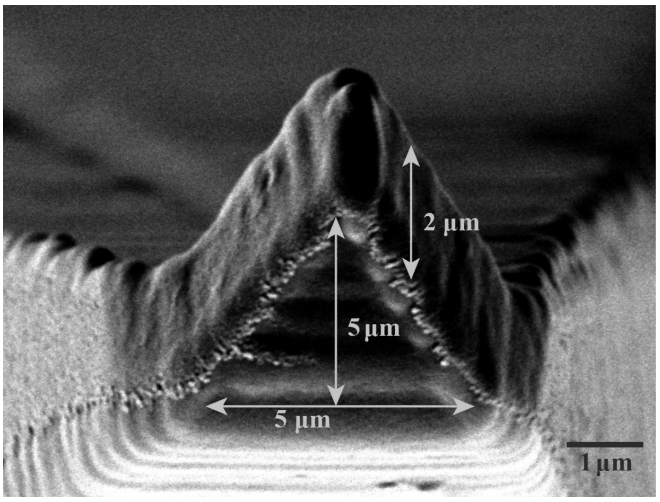

Fig. 2.5. SEM image of the hybrid tip containing the dimensions of the miniaturised loop.

By identifying the local RF voltage $\underline{U}$ and current $\underline{I}$, from equations Equations (2.7) & (2.8), parasitic contributions captured in $\underline{U}_{\text{lin}}$, and $\underline{I}_{\text{lin}}$ can be eliminated. As the tip-circuit distance is continously increased during a measurement, a complex fit can be decomposed to identify the magnitude and phase of both the linear, and non-linear components. As such, both the magnitude and phase of local RF voltage $\underline{U}$ and current $\underline{I}$ can be identified.

IV. Probe Characterisation

In order to validate the novel fabrication process for the application of contactless RF voltage and current probes, a Scanning Electron Microscope (SEM) (JSM-6010LA, JEOL Ltd., Japan) has been employed. It allows for geometrical inspection with nm-resolution, making it suitable for determining the tip apex radius, and the dimensions of the conductive loop. As shown earlier in Equations (2.5) & (2.6) these dimensions play an important role in predicting the spatial resolution.

A. Functional Design Elements

As mentioned the area enclosed by the conductive loop, and tip apex radius of the sharp conductive tip, determine the spatial resolution that can be achieved with the probe. Hence, a SEM inspection has been conducted to verify these dimensions, and thus estimate the spatial resolution that can be achieved with the probe. Furthermore, the electrical isolation between the two transmission lines has been verified, and will be discussed in Chapter 3.

The sharp conductive tip as shown in Fig. 2.4 has a tip apex radius of approximately $100\,\text{nm}$, resulting in an effective tip apex radius of $R_{\text{eff}} \approx 1\,\mu\text{m}$. According to Equation (2.5) this allows for measurements with µm-resolution. However, the tip sits on a small plane, which will act as a parallel plate capacitor, deteriorating the spatial resolution.

The dimensions of the triangular conductive loop as depicted in Fig. 2.5 show the dimensions where the base and height are both equal to $5\,\mu\text{m}$, hence, the loop encloses an area of $12.5\,\mu\text{m}^2$, where the loop has a constant width of $2\,\mu\text{m}$.

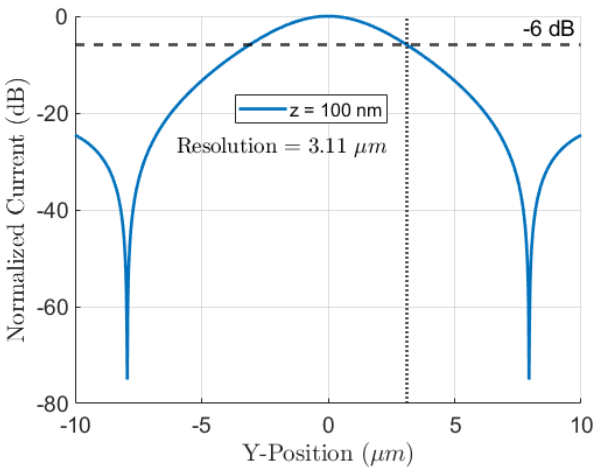

Fig. 2.6. Cross-sectional current simulation, at a tip-sample distance of $z = 100\,\text{nm}$, showing a simulated spatial resolution of approximately $3.11\,\mu\text{m}$.

B. Inductive Coupling Simulations

The spatial resolution that can be achieved with the loop dimensions has been evaluated with simulations that do not employ the model-based approach, so that the probe fabrication method can be compared to conventional techniques. The method of determining the spatial resolution as presented in [20] has been employed. In the simulations, the tip-circuit distance is kept constant while the probe is moved over a cross-section of a Microstrip that functions as the DUT. The spatial resolution is determined as the coordinate where the normalised signal crosses the $-6\,\text{dB}$ threshold. Adjusting the DUT and tip-circuit distance influences this value. With the probing setup presented in Fig. 2.3, tip-circuit distances as small as $100\,\text{nm}$ can be achieved. As can be seen from Fig.

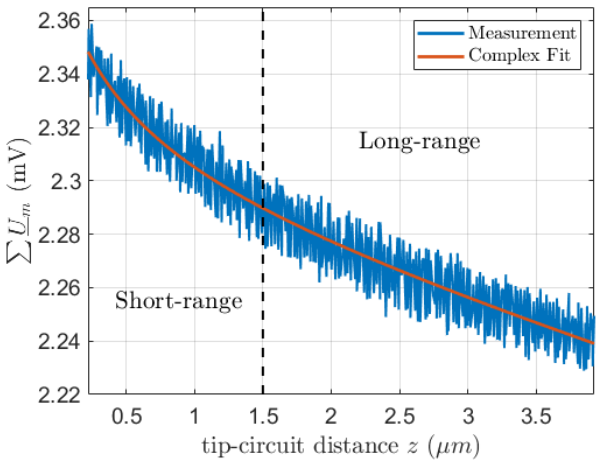

Fig. 2.7. Model-based complex fitting to a common-mode potential vs. tip-circuit distance measurement, where there can be distinguished between short-, and long-range distance dependencies.

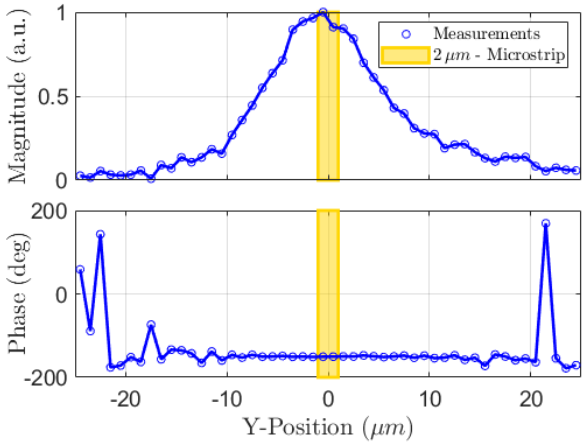

Fig. 2.8. Contactless RF voltage measurement at a frequency of 10 GHz according to the model-based approach [7] over a cross-section of a microstrip.

2.6, it is estimated from simulations that at this tip-circuit distance, a spatial resolution of 3.11 µm can be expected.

V. Contactless RF Measurements On A Transmission Line

To demonstrate the effectiveness of the newly designed contactless RF probe, multiple measurements have been performed on an open-ended Microstrip transmission line, that acted as the DUT. As the open-end will have an impedance mismatch it is assumed that the signal is fully reflected, leading to standing waves. The microstrip comprises a 2 µm-wide conductor, that is fully encapsulated by a passivation layer with a relative permittivity $\varepsilon_r = 4.0$. From the conductor, the passivation layer has a thickness of 2 µm to the surface of the DUT, and approximately 5 µm to the ground plane at the bottom of the Microstrip. By applying the model-based approach to a measurement over a cross-section of the Microstrip the spatial resolution of the probe can be evaluated. Next to that, the probe can be positioned in a fixed location while the frequency is sweeped to evaluate the measurement bandwidth.

A. Cross-Sectional Measurement

The model-based approach as earlier described in Section III-B is applied to conduct a measurement over the Y-coordinate as indicated in Fig. 2.3. In order to apply the model-based approach a short-range nonlinear tip-circuit distance dependency needs to be distinguishable. In Fig. 2.7 such a $\sum \underline{U}_\mathrm{m}$ versus tip-circuit distance measurement is shown, where the data is used to perform a complex fit. It can be seen that the short-range signal ($z < 1.5$ µm) contains a non-linear component, whereas the long-range signal is dominated by an approximately linear tip-circuit distance dependency. Performing these fitting procedures has been successful for contactless RF voltage measurements, however as of yet, there has been no success in extending the model-based approach to contactless RF current measurements.

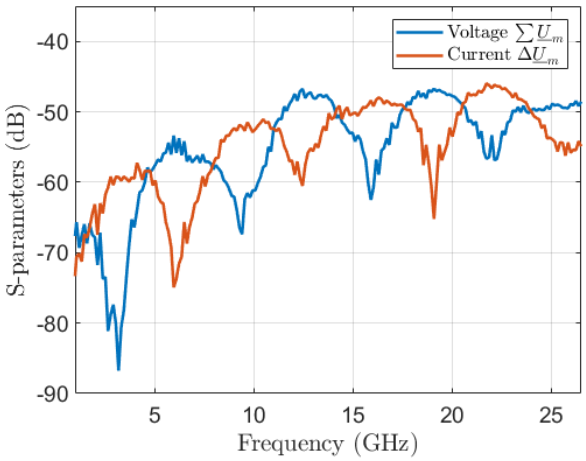

Fig. 2.9. A contactless RF voltage, and current measurement where the probe is kept at a fixed position, approximately 10 µm above the DUT.

The model-based approach has been employed for multiple measurements over a cross-section of the microstrip, leading to the voltage distribution depicted in Fig. 2.8. From here the spatial-resolution of the probe can be evaluated. As there is no standardized method to determine the spatial-resolution, this research defines it as the Y-coordinate where the normalised signal crosses the −6 dB threshold. The spatial-resolution is therefore approximately equal to 8 µm.

B. Stationary Contactless Measurement

A second measurement is performed where the probe is kept above the microstrip at a fixed tip-circuit distance of approximately 10 µm. The frequency is continuously increased from 1 to 26.5 GHz, while both the common-mode-, and differential mode potential are measured. It is expected from Equations (2.1) & (2.2) that both the common-mode and differential-mode potential show a linear increase with frequency. Due to the standing waves resulting from the open-ended transmission

line, the voltage and current will increase with frequency showing alternating polarities. Hence, the graphs represented in Fig. 2.9 confirm that the common-mode, and differential-mode potential represent the RF voltage and current respectively.

It is assumed that the bandwidth of the probe is limited by reflected signals due to an impedance mismatch at the interface between the probe and PCB. When the length between this interface and the probe-tip approaches the quarter wavelength ($\lambda/4$) of the measured signal, reflections will become more significant. Therefore minimizing the length of the signal path will result in a larger bandwidth [7]. When the signal path has a length equal to $\lambda/4$, an anti-resonance will be observed, as the probe will act as a quarter wavelength attenuator. The length of the signal path lies in the range of $5\,\mathrm{mm}$ to $2\,\mathrm{mm}$, as the exact location where the signal passes through the contact pads that form the probe-PCB interface is unclear. The highest measurement frequency that can be achieved with this probe therefore lies between 15 and $37.5\,\mathrm{GHz}$. At a frequency of $23\,\mathrm{GHz}$ curve flattening can be made out from the voltage measurement. The contactless RF probe therefore has a characterised measurement bandwidth ranging from 1 to $23\,\mathrm{GHz}$.

VI. Conclusion

In this paper the model-based approach presented in [7] has been expanded to conduct both contactless local RF voltage and current measurements. The probe is manufactured in a novel fabrication process for the application of multi-component near-field probes, or contactless RF voltage and current probes. It resulted in a sharp conductive tip with a tip apex radius of $100\,\mathrm{nm}$, that sits on top of a miniaturised triangular conductive loop that encloses an area of $12.5\,\mu\mathrm{m}^2$. The simulated spatial resolution for contactless RF current measurements according to the criteria presented in [20] was found to be $3.11\,\mu\mathrm{m}$. The model-based approach has been applied to a contactless RF voltage measurement over a cross-section of a Microstrip, where a spatial resolution of $8\,\mu\mathrm{m}$ was determined according to the method provided in [20]. The bandwidth of the probe has been determined by conducting a stationary contactless measurement. The probe was positioned $10\,\mu\mathrm{m}$ above the microstrip, while the signal frequency on the DUT was increased. Both the common-mode potential and differential-mode potential were measured. Curve flattening was observed with contactless voltage measurements at frequencies above $23\,\mathrm{GHz}$. The probe can hence be employed for contactless RF voltage and current measurements that lie in a bandwidth of 1 to $23\,\mathrm{GHz}$.

VII. Experimental Section

In this section, the fabrication process is presented, in which a multiscale 3D-printing approach has been optimised in combination with a thermal evaporation process in order to fabricate probes capable of contactless RF voltage and current measurements. The measurement procedure for performing contactless model-based RF voltage [7] and current measurements is also discussed.

TABLE 2.1
Printing parameters used in the 2PP process.

	Base	Cantilever	Sensing Tip
Laser power*	$40\,\%$	$50\,\%$	$30\,\%$
Scanning speed ($\mathrm{mm\,s^{-1}}$)	10	40	7
Slicing distance (µm)	0.3	0.2	0.1
Hatching distance (µm)	0.3	0.2	0.1
Galvo acceleration ($\mathrm{V\,ms^{-2}}$)	5	5	1

* Given as the percentage of the total laser power of $50\,\mathrm{mW}$

A. Fabrication Process

As mentioned before in Section II a multiscale 3D-printing process is used to fabricate the probe substrate. The chip body is printed with a DLP-printer (Micro2, microSLA, USA) in combination with a compatible high-resolution resin (UHR, microSLA, USA). The step height in the Z-direction is set to $1\,\mu\mathrm{m}$, while the XY-resolution is set to $5\,\mu\mathrm{m}$. The prints are cleaned in IPA ($99.8\,\%$ Honeywell, Riedel-de-Haën, Germany) in two subsequent steps of $2\,\mathrm{min}$ each.

To align the chip-bodies in the 2PP setup, a chip-body holder is 3D-printed in a DLP-printer (Micro Plus HiRes, EnvisionTEC GmbH, Germany) with an XYZ-resolution of $35\,\mu\mathrm{m}$, in combination with their compatible photoresist (HTM140v2, EnvisionTEC GmbH, Germany). The resulting structure including supports is cleaned in an ultrasonic cleaner using IPA ($99.8\,\%$ Honeywell, Riedel-de-Haën, Germany) before post-exposure curing it in a UV-oven at $80\,^{\circ}\mathrm{C}$ in combination with UV-light for $20\,\mathrm{min}$. During the curing step, it is clamped between two microscope-slides. Lastly, the 3D-printing supports are removed.

The chip-bodies are placed in the 3D-printed chip-body holder, which are subsequentially loaded into a designated 9x9 sample holder. Prior to loading the 9x9 holder into the 2PP-setup (Photonic Professional GT Laser Lithography System, Nanoscribe GmbH, Germany), a high-resolution resin (IP-Dip, Nanoscribe GmbH, Germany) is deposited on the chip-bodies in the desired printing locations. The 2PP printing-process is optimised for each distinct part as noted in Table 2.1. At the start of the printing process, the interface of the chip-body is manually identified, and the laser of the 2PP system focused approximately $5\,\mu\mathrm{m}$ below the surface. All parts are printed in the 63x magnification DiLL configuration. The samples are developed in two steps. In the first step, they are submerged for $5\,\mathrm{min}$ in propylene-glycol-methyl-ether-acetate (PGMEA, Sigma– Aldrich, USA), and subsequentially another $20\,\mathrm{min}$ in IPA ($99.8\,\%$ Honeywell, Riedel-de-Haën, Germany).

In the next fabrication step, the probes are mounted in a thermal evaporator (Temescal FC-2000, Ferrotec USA, USA). To deposit a Titanium (Ti) thin film of $10\,\mathrm{nm}$, the chamber is first evacuated to a pressure of $2\,\mathrm{mTorr}$. While the sample holder is rotating at a speed of $10\,\mathrm{RPM}$, the material is deposited with a deposition rate of $0.5\,\mathrm{\AA\,s^{-1}}$. In the subsequent deposition step, a $100\,\mathrm{nm}$ Gold (Au) thin film is deposited at a pressure of $3\,\mathrm{mTorr}$. The sample holder again rotates with $10\,\mathrm{RPM}$, while the deposition rate is kept at $1.0\,\mathrm{\AA\,s^{-1}}$.

Handling the resulting probes is critical, and has to follow Electrostatic Discharge (ESD)-rules. In the final fabrication

step, the probes are carefully aligned to the PCBs with the assistance of the alignment hemispheres. The sides of the probes are then glued (Loctite 401, Henkel AG & Co. KGaA, Germany) to the PCB, yielding the final probe-PCB assembly.

B. Measurement Procedure

The measurement procedure is similar to the one presented in [7]. The PCB-probe assembly is first mounted in the modified AFM-setup. The focus of the read-out laser is then aligned to the end of the cantilever, so that the signal of the reflected beam on the photodiode is maximised. The SMA-connectors on the PCB-probe assembly, and GSG contact probe, now need to be connected to the VNA.

An optical microscope and stepper motors are used for the alignment in XY-directions, and to approach the surface of the circuit. The more accurate vertical piezo is actuated to identify the circuit interface, such that the probe approaches the circuit with constant velocity. As the probe makes mechanical contact the cantilever deflects, which is detected by the photodiode. However, for the contactless measurements, only distances $z > 100\,\mathrm{nm}$ are considered, hence, contactless RF measurements can be performed.

During a measurement, the DUT receives a signal from the VNA through the GSG contact probe. The contactless RF probe is now positioned over the DUT in a certain XY-coordinate. Both the common-mode potential, and the differential-mode potential are continuously measured while the tip-circuit distance is increased. To eliminate parasitic contributions to the signal the model-based approach as presented in Section III-B can be applied to identify the local RF voltage $\underline{U}$ and current $\underline{I}$.

REFERENCES

[1] Y.-C. Chang, P.-Y. Wang, D.-C. Chang, and S.-S. Hsu, "A low-loss fully integrated cmos active probe for gigahertz conducted emi test," *IEEE Transactions on Microwave Theory and Techniques*, vol. 67, no. 4, pp. 1652–1660, 4 2019.

[2] M. Poik, T. Hackl, S. Di Martino, M. Schober, J. Dang, and G. Schitter, "Analysis of cross-talk induced measurement errors in model-based rf voltage sensing," in *2023 IEEE International Instrumentation and Measurement Technology Conference (I2MTC)*, 2023, pp. 1–6.

[3] A. Rumiantsev and R. Doerner, "Rf probe technology: History and selected topics," *IEEE Microwave Magazine*, vol. 14, no. 7, pp. 46–58, 2013.

[4] V. Solomko, O. Özdamar, R. Weigel, and A. Hagelauer, "Model of substrate capacitance of mosfet rf switch inspired by inverted microstrip line," in *51st IEEE European Solid-State Device Research Conference (ESSDERC)*. Grenoble, France: IEEE, 9 2021, pp. 207–210.

[5] S. Ziegler, R. C. Woodward, H. H.-C. Iu, and L. J. Borle, "Current sensing techniques: A review," *IEEE Sensors Journal*, vol. 9, no. 4, pp. 354–376, 4 2009.

[6] O. Özdamar, A. M. Hagelauer, R. Weigel, and V. Solomko, "An rf voltage detector with low harmonic feedback for antenna tuning switches," in *2019 IEEE International Conference on Microwaves, Antennas, Communications and Electronic Systems (COMCAS)*. Tel-Aviv, Israel: IEEE, 2019, pp. 1–5.

[7] M. Poik, T. Hackl, S. Di Martino, B. M. Berger, S. W. Sattler, and G. Schitter, "A contactless method for measuring amplitude and phase of rf voltages up to 26.5ghz," *IEEE Sensors Journal*, 2024.

[8] W. Fang, H. Qiu, C. Luo, L. Wang, and E. Shao, "Noncontact rf voltage sensing of a printed trace via a capacitive-coupled probe," *IEEE Sensors Journal*, vol. 18, no. 21, pp. 8873–8882, 11 2018.

[9] R. Kantor and I. V. Shvets, "Measurement of electric-field intensities using scanning near-field microwave microscopy," *IEEE Transactions on Microwave Theory and Techniques*, vol. 51, no. 11, pp. 2228–2234, 11 2003.

[10] R. Hou, M. Spirito, R. Heeres, F. van Rijs, and L. C. N. de Vreede, "Non-intrusive near-field characterization of distributed effects in large-periphery ldmos rf power transistors," in *2015 IEEE MTT-S International Microwave Symposium (IMS)*. IEEE, 2015, pp. 1–3.

[11] N. Dehghan and S. C. Cripps, "A novel in-situ calibration technique for a high resolution e-field probe," in *2015 IEEE MTT-S International Microwave Symposium (IMS)*. Phoenix, AZ, USA: IEEE, 3 2015, pp. 1–3.

[12] Y. T. Chou and H. C. Lu, "Space difference magnetic near-field probe with spatial resolution improvement," *IEEE Transactions on Microwave Theory and Techniques*, vol. 61, no. 12, pp. 4233–4244, 12 2013.

[13] Z. Yan, W. Liu, J. Wang, D. Su, X. Yan, and J. Fan, "Noncontact wideband current probes with high sensitivity and spatial resolution for noise location on pcb," *IEEE Transactions on Instrumentation and Measurement*, vol. 67, no. 12, pp. 2881–2891, 12 2018.

[14] H. Qiu, W. Fang, Y. En, Y. Huang, Y. Liu, P. Lai, Y. Chen, and C. Shi, "Movable noncontact rf current measurement on a pcb trace," *IEEE Transactions on Instrumentation and Measurement*, vol. 66, no. 9, pp. 2464–2473, 9 2017.

[15] N. Ando, N. Masuda, N. Tamaki, T. Kuriyama, K. Kato, M. Saito, S. Saito, K. Ohashi, and M. Yamaguchi, "Miniaturized thin-film magnetic field probe with high spatial resolution for lsi chip measurement," New Industry Creation Hatchery Center (NICHe), Tohoku University, Tech. Rep., 2004.

[16] J. Wang, Z. Yan, J. Liu, Y. Zhou, C. Fu, and D. Su, "Miniature active differential magnetic field probe with high sensitivity for near-field measurements," *IEEE Transactions on Antennas and Propagation*, vol. 70, no. 2, pp. 1575–1580, 2 2022.

[17] W. Shao, Y. Chen, L. Huang, and W. Fang, "An asymmetric correction method for differential double-loop magnetic field probing system," *IEEE Transactions on Antennas and Propagation*, vol. 71, no. 10, pp. 6349–6354, 2023.

[18] G. Li, W. Shao, R. Chen, Y. Zhang, and Z. Wang, "Ultrawideband differential magnetic near field probe with high electric field suppression," *IEEE Sensors Journal*, vol. 20, no. 14, pp. 7669–7676, 7 2020.

[19] R. Yang, X.-C. Wei, Y.-F. Shu, D. Yi, and Y.-B. Yang, "A miniature multi-component probe for near-field scanning," *IEEE Transactions on Antennas and Propagation*, vol. 67, no. 11, pp. 6821–6828, 11 2019.

[20] L. Wang, X. Liu, W. Shao, and Z. Zhu, "An ultrawideband four-port composite probe with simultaneous measurement of multicomponent fields and improvement of electric-field suppression," *IEEE Transactions on Components, Packaging and Manufacturing Technology*, vol. 13, no. 8, pp. 1278–1286, 8 2023.

[21] W. Shao, W. Fang, Y. Huang, Z. Liu, and X. Dong, "Simultaneous measurement of electric and magnetic fields with a dual probe for efficient near-field scanning," *IEEE Transactions on Antennas and Propagation*, vol. 67, no. 4, pp. 2859–2864, 4 2019.

[22] C. Luo, W. Fang, Y. Shen, H. Qiu, F. Yu, and H. Li, "Collocated and simultaneous measurements of rf current and voltage on a trace in a noncontact manner," *IEEE Transactions on Microwave Theory and Techniques*, vol. 67, no. 6, pp. 2406–2415, 6 2019.

[23] W. Shao, Z. Yi, X. He, W. Fang, C. Zhou, and J. Liu, "Novel calibration method for the asymmetric probing in the near-field measurement with a dual probe," *IEEE Transactions on Microwave Theory and Techniques*, vol. 69, no. 12, pp. 5439–5448, 12 2021.

[24] W. Shao, J. Li, Q. Huang, E. Shao, and J. Liu, "A two-turn loop active magnetic field probe design for high sensitivity near-field measurement," *IET Science, Measurement & Technology*, vol. 16, no. 1, pp. 40–49, 1 2022.

[25] M. Poik, T. Hackl, S. D. Martino, M. Schober, J. Dang, and G. Schitter, "Model-based rf sensing for contactless high-resolution voltage measurements," *IEEE Transactions on Instrumentation and Measurement*, vol. 72, pp. 1–8, 2023.

[26] O. H. Olubowale, S. Biswas, G. Azom, B. L. Prather, S. D. Owoso, K. C. Rinee, K. Marroquin, K. A. Gates, M. B. Chambers, A. Xu, and J. C. Garno, ""may the force be with you!" force-volume mapping with atomic force microscopy," *ACS Omega*, vol. 6, no. 40, pp. 25 860–25 875, 2021.

[27] M. Blankespoor, T. Manzaneque, and M. K. Ghatkesar, "Discrete femtolitre pipetting with 3d printed axisymmetrical phaseguides," *Small Methods*, vol. 8, no. 3, p. 2300942, 3 2024.

[28] R. C. Kramer, E. J. Verlinden, L. Angeloni, A. van den Heuvel, L. E. Fratila-Apachitei, S. M. van der Maarel, and M. K. Ghatkesar, "Multiscale 3d-printing of microfluidic afm cantilevers," *Lab on a Chip*, vol. 20, no. 2, pp. 311–319, 1 2020.

[29] P. F. J. van Altena, "Multiscale 3d printed polymer probes for single cell experiments," Master's thesis, TU Delft, 2021.

[30] L. Fumagalli, G. Ferrari, M. Sampietro, I. Casuso, E. Martinez, J. Samitier, and G. Gomila, "Nanoscale capacitance imaging with attofarad resolution using ac current sensing atomic force microscopy," *Nanotechnology*, vol. 17, no. 18, pp. 4581–4587, 9 2006.

3

Skewed Grooves for 3D-Printed Non-Planar Circuits

The probe design required a method of creating multiple transmission lines on top of a single 3D-printed non-planar surface. A method with these capabilities has not only been devised, but also patented. The techniques described in the literature are often limited to planar structures, or require numerous fabrication steps and machines. Therefore this work presents a two-step fabrication process, 3D-printing followed by Physical Vapor Deposition (PVD), that results in mutually isolated signal paths that are geometrically overlapping in their projected geometry.

3.1. Literature

The literature describes a variety of fabrication processes that result in non-planar metallic patterns. However, these methods all have certain shortcomings that we believe our newly proposed technique overcomes.

A common patterning technique is shadow (mask) evaporation [1]. The technique makes use of a thermal evaporation process where material is vaporized in an evacuated chamber and condenses on a substrate, forming a thin film. During this process, the material vapour travels in an approximately straight line from the source to the substrate and can be physically blocked with a mask to create a pattern on the substrate [2].

A mask can either be a separate, movable structure or be fixed to the substrate [2]. Flexible masks have been used to pattern non-planar substrates [3]. Although non-planar substrates have been patterned with this technique, the resulting patterns have gaps between the features. These can be eliminated with our newly proposed technique, resulting in less chip area consumption. Another problem with fixed masks is the material deposited inside the negative features. If this material is not electrically connected, it will form an undefined electrical plane. These planes are often affected by Electrostatic Discharge (ESD), which can damage or even destroy the chip.

Lift-off patterning is another widely used technique. A substrate is first patterned using lithography, where it is coated with a layer of resist. A pattern is then exposed by a photon or electron beam, changing the chemical composition of the illuminated area, making it either more or less soluble, depending on the type of resist. After exposure, the soluble material is removed, leaving behind a patterned substrate. A thin film is deposited on top of the patterned substrate, resulting in a thin film on both the substrate and the hardened resist. In the final step, the hardened resist covered with a thin film is chemically removed or lifted off the substrate, leaving only the thin film that is deposited directly on the substrate. [4]–[7]

This technique produces planar patterns, but techniques have been developed to transfer these planar patterns onto non-planar surfaces [4]–[6]. These techniques require multiple substrates: a patterned substrate, a transfer substrate, and a target substrate [5], [6]. The patterned substrate is first patterned

according to conventional lift-off patterning. The pattern is then transferred to a flexible transfer substrate by pressing the patterned substrate and transfer substrate against one another. The flexible transfer substrate is then pressed onto a non-planar target substrate for the final transfer, resulting in a patterned non-planar target substrate.

The substrates are optically aligned with each other during the transfer process, which makes this technique unsuitable for applications requiring high repeatability. Additionally, there have been reports of adhesion problems, resulting in features that are not transferred or become wrinkled during transfer steps. While the resolution of the process is limited only by the resolution of the lithography process, the technique still results in features with gaps in between where the hardened resist is lifted off the substrate, which can be regarded as wasted area on the chip.

3.2. Invention Description

The invention describes a patterning technique for fabricating signal paths on 3-dimensional surfaces and devices. It consists of only 2 fabrication steps: 3D printing, followed by PVD.

The first fabrication step is 3D-printing. A skewed-groove is integrated into an arbitrary non-planar surface to be patterned. The groove then acts as a separation between the electrically conductive planes/lines that are formed in the thermal evaporation process. A cross-section of such a skewed-groove, and the direction of thermal evaporation is depicted in Figure 3.1.

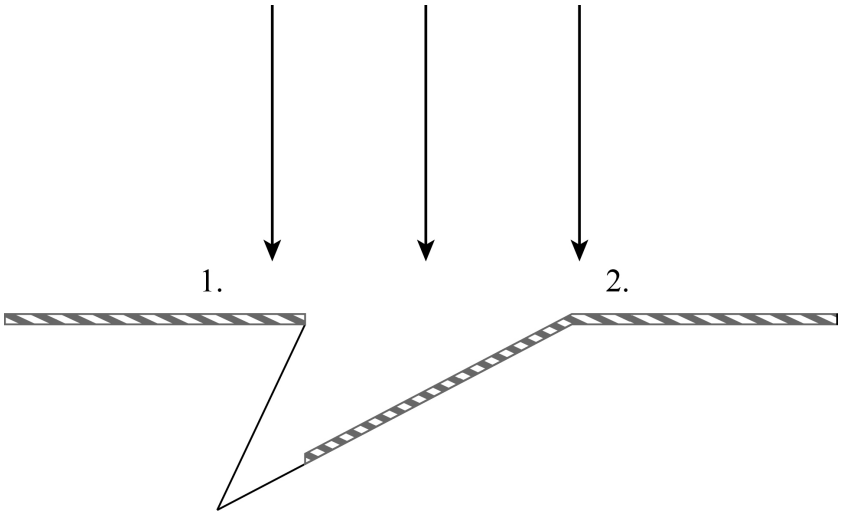

Figure 3.1: Schematic cross-section showing the orientation during the PVD process, and the resulting mutually isolated films (1 & 2)

In the second fabrication step, the 3D-printed structures are mounted in a PVD system, such that the bottom of the grooves have no direct sight of view to the source material of the PVD system. PVD processes can be used to deposit a thin layer of material (e.g. a metal, or a piezoelectric ceramic) on a structure. The material is subsequentially ejected from the source and travels in an approximately straight line to the structure where it accumulates on the surface, forming a thin film. The skewness of the grooves prevents an electrical connection between the deposited thin films on the planes (1 & 2), as it forms a physical seperation. The resulting structure will hence, feature two mutually isolated, but electrically conductive thin films that are overlapping in their projected geometry.

3.3. Experimental Verification

The technique is experimentally verified with two printing techniques: Digital Light Processing (DLP) stereolithography printing, and Two Photon Polymerisation (2PP) printing. Figure 3.2 Shows a Scanning Electron Microscopy (SEM) image of a DLP-printed non-planar substrate that is patterned with a skewed-groove.

In the example a DLP printer (Micro2, MicroSLA, USA; UHR Resin, MicroSLA, USA) is used. This

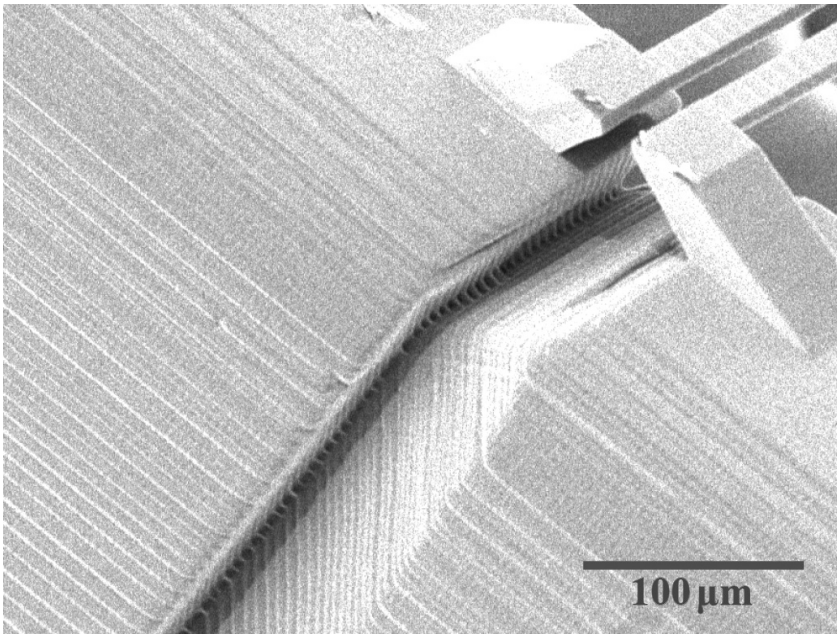

Figure 3.2: SEM image of a DLP printed 3D-application of the skewed groove showcasing its effectiveness in patterning of electrically isolated films on 3D-substrates.

printer has an XY-resolution of $5\,\mu\mathrm{m}$, and can print layers with a thickness down to $1\,\mu\mathrm{m}$ in the Z-direction. Another test is done with a higher resolution 2PP printer (Photonic Professional GT Laser Lithography System, Nanoscribe GmbH, Germany; IP-Dip Resin, Nanoscribe GmbH, Germany) which is configured in the Dip-in Laser Lithography (DiLL) mode. It yielded similar results, however finding the right printing parameters is more time-consuming, as it is an iterative optimisation process. The writing parameters such as laser power and scan speed need to be optimised for different environments and geometries.

The resulting electrical isolation is verified with a 4-point probing station (PM5 Probing Station, Süss MicroTec GmbH, Germany). The probes are connected to a Source / Measurement Unit (SMU) (B2912A Precision SMU, Keysight Technologies, USA). When the 4-point probe is connected as depicted in Figure 3.3a, a current could be measured. Whereas in the configuration as depicted in Figure 3.3b, no current could be detected due to the separation formed by the skewed-groove.

3.4. Considerations

With any technique, there are certain considerations that need to be taken into account. Surface smoothness of the 3D-printed structure is one such important parameter, affecting the step-coverage. It can be overcome by sufficient surface diffusion in the PVD-process. Time-varying signals transmitted through the patterned surface will be subjected to self-capacitance. Outgassing is another effect that needs to be considered during the PVD-process, as it can compromise the integrity of the vacuum system and clean room.

3.4.1. Surface Diffusion

Surface diffusion is one of the effects that occurs during the thermal evaporation process, and can influence the thin film deposition process. Evaporated atoms that reach the substrate can move around the surface through diffusion. During this process, atoms diffuse to the energetically favouring positions [8]. More diffusion can lead to more uniform film growth.

The skewed groove patterning technique makes use of a 3D-printed substrate. Sufficient surface smoothness is required such that the step-coverage can be overcome. Techniques where the deposited atoms have a high landing energy, are favourable as the diffusion ensures there are no disconnections in the electrically conductive thin film. A negative feature or undercut is also subjected to effects of

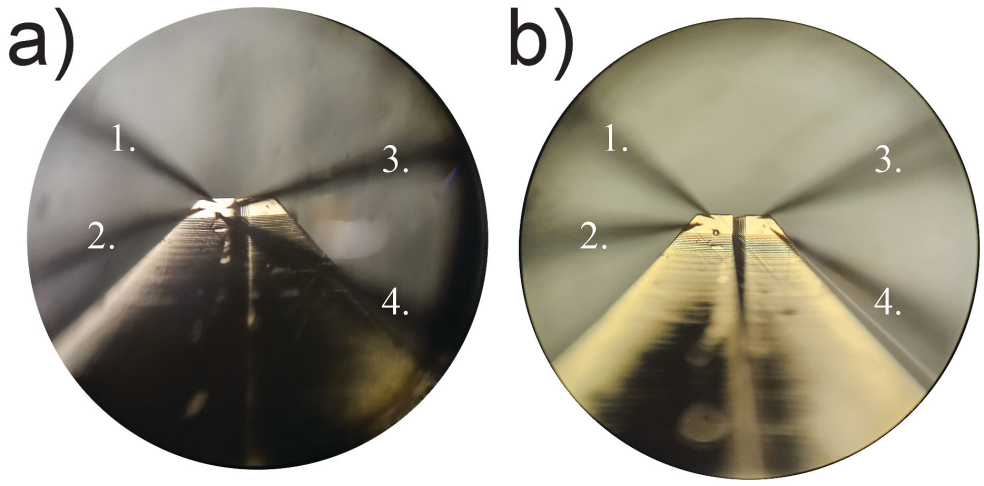

Figure 3.3: Photographs of the measurement setup where the probe arms are depicted by: 1 high force, 2 high sense, 3 low force, and 4 low sense. In configuration a) a current can be detected, and in configuration b) no current can be detected as a result of the skewed groove.

diffusion [9]. Therefore thin film 2 depicted in Figure 3.1 will continue slightly underneath film 1 due to surface diffusion, leading to two electrically conductive films that are overlapping in their projected geometry.

3.4.2. Self-Capacitance

The proposed technique can be applied to a variety of different applications. When these require time-varying signals to be transmitted through patterns created with skewed-grooves, self-capacitance as depicted in Figure 3.4 needs to be taken into account. A good understanding of this capacitance is crucial for preventing unwanted parasitic coupling between the electrically isolated films 1 and 2 as depicted in Figure 3.1, which can act as an electrical short when not properly considered.

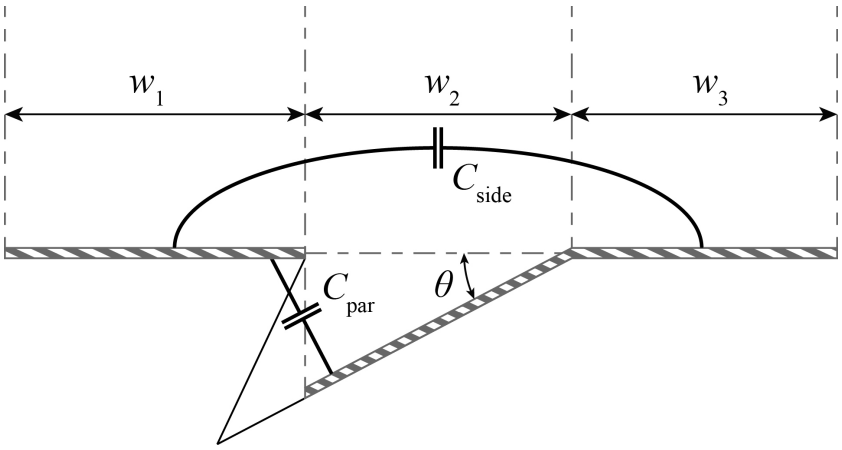

Figure 3.4: Schematic cross section containing geoemetric variables, and the contributions to the self-capacitance.

There are two main contributors to the self-capacitance. The conductive film deposited inside of the groove can be approximated as an inclined parallel plate capacitor with capacitance C_{par}. The conductive films that are deposited in the same plane can be approximated by a radial model as described in [10] to find C_{side}. The total self-capacitance is approximately equal to $C_{\text{tot}} \approx C_{\text{par}} + C_{\text{side}}$. They can be calculated according to the equations depicted below:

$$C_{\text{par}} = \frac{\varepsilon_0 \, \varepsilon_r \, L}{\tan(\theta)} \ln\left(1 + \tan^2 \theta\right) \tag{3.1}$$

$$C_{\text{side}} = \frac{\varepsilon_0 \, \varepsilon_r \, L}{\pi} \ln\left(1 + 2 \, \frac{\min(w_1, w_3)}{w_2}\right) \tag{3.2}$$

The variables ε_0, ε_r, and L denote the permittivity in free space, the relative permittivity, and the length of the groove respectively. The remaining geometrical variables are defined in Figure 3.4.

3.4.3. Outgassing

Most 3D-printing techniques make use of polymeric materials. These are subjected to outgassing, which can make them incompatible with vacuum systems[11], [12]. The thermal evaporator used in the experimental verification for example makes use of a vacuum chamber. A good understanding of what happens during outgassing is therefore crucial, to ensure the integrity of the vacuum chamber is not compromised. During their fabrication, polymers can absorb and trap gasses, water, and volatile substances. When exposed to low-pressure environments these substances can migrate to the surface and escape [11].

The rates at which polymers are outgassing depend on their geometry and environment [11], [12]. A higher surface-to-volume ratio leads to less outgassing, therefore smaller polymeric structures are less likely to be subjected to outgassing. The environmental conditions also have an influence on outgassing rates. Due to the low pressure in a vacuum chamber, outgassing rates increase [11]. Similarly, outgassing rates also increase with temperature [12].

3.5. Applications

In this research, the technique is applied for RF sensing purposes. A loop structure connects two transmission lines that are separated by a skewed-groove. When placed in a time-varying magnetic field a potential difference over the loop could be detected, proportional to the area enclosed by the loop. Since the planes of the patterned structures are geometrically overlapping they span no area in the sensing direction. Therefore they would induce less noise for RF-magnetic field sensing applications, with the drawback that they are subjected to self-capacitance which was touched upon in Section 3.4.2.

Next to this, there are a variety of applications that could make use of a 3D-patterning technique that results in planes that are overlapping in their projected geometries. Complex 3-dimensional integrated circuits (ICs) can be realised with the technique, where different types of circuits are integrated into one. Energy-, and memory storage techniques could also benefit from the proposed patterning technique as geometrically overlapping planes allow for even more compact designs with complex 3-dimensional geometries. The technique could be applied for implant technologies as bio-compatible resins can be 3D-printed into complex structures that are optimised for the specific application.

In conclusion, there are many applications where the proposed technique can be utilised. In this research, only a few are highlighted, but in reality, through creative thinking and innovation, many more applications can be explored. This technique poses another great option in the scala of patterning techniques that can be applied with its own unique benefits and limitations.

Invention References

[1] M. Luitz, M. Lunzer, A. Goralczyk, *et al.*, “High resolution patterning of an organic–inorganic photoresin for the fabrication of platinum microstructures,” *Advanced Materials*, vol. 33, no. 37, p. 2 101 992, 2021.

[2] T. Schallenberg, C. Schumacher, S. Gundel, and W. Faschinger, “Shadow mask technology,” *Thin Solid Films*, vol. 412, no. 1-2, pp. 24–29, Jun. 2002.

[3] J. H. Choi and G. M. Kim, “Micro-patterning on non-planar surface using flexible microstencil,” *International Journal of Precision Engineering and Manufacturing*, vol. 12, no. 1, pp. 165–168, 2011.

[4] H. Mitomo and K. Ijiro, “Controlled nanostructures fabricated by the self-assembly of gold nanoparticles via simple surface modifications,” *Bulletin of the Chemical Society of Japan*, vol. 94, no. 4, pp. 1300–1310, Apr. 2021.

[5] K. J. Lee, K. A. Fosser, and R. G. Nuzzo, “Fabrication of stable metallic patterns embedded in poly(dimethylsiloxane) and model applications in non-planar electronic and lab-on-a-chip device patterning,” *Advanced Functional Materials*, vol. 15, no. 4, pp. 557–566, Apr. 2005.

[6] E. J. Smythe, M. D. Dickey, G. M. Whitesides, and F. Capasso, “A technique to transfer metallic nanoscale patterns to small and non-planar surfaces,” *ACS Nano*, vol. 3, no. 1, pp. 59–65, 2009.

[7] M. Zheng, Y. Yang, P. Liu, H. Duan, P. D. Keathley, and K. K. Berggren, “Fabrication of gold nanostructures using wet lift-off without adhesion promotion,” *Microelectronic Engineering*, vol. 233, p. 111 420, Sep. 2020.

[8] L. Abelmann, “Oblique evaporation and surface diffusion,” *Thin Solid Films*, vol. 305, pp. 1–21, 1997.

[9] B. Cord, C. Dames, K. K. Berggren, and J. Aumentado, “Robust shadow-mask evaporation via lithographically controlled undercut,” *Journal of Vacuum Science & Technology B: Microelectronics and Nanometer Structures*, vol. 24, no. 6, pp. 3139–3143, Nov. 2006.

[10] A. Bansal, B. C. Paul, and K. Roy, “An analytical fringe capacitance model for interconnects using conformal mapping,” *IEEE Transactions on Computer-Aided Design of Integrated Circuits and Systems*, vol. 25, no. 12, pp. 2765–2774, Dec. 2006.

[11] R. Grinham and A. Chew, “A review of outgassing and methods for its reduction,” *Applied Science and Convergence Technology*, vol. 26, no. 5, pp. 95–109, Sep. 2017.

[12] K. Battes, C. Day, and V. Hauer, “Outgassing behavior of different high-temperature resistant polymers,” *Journal of Vacuum Science & Technology A: Vacuum, Surfaces, and Films*, vol. 36, no. 2, p. 021 602, Mar. 2018.

4

Thesis Conclusion

To gain a broad understanding of the scientific field, a literature survey is conducted in the field of near-field scanning technologies. From there a variety of probes are reviewed. It is found that the electric and magnetic fields that are emitted by integrated circuits operating at radiofrequencies can be measured and analysed in order to locally characterise voltage and current distributions in these circuits. Probes described in the literature are often fabricated through PCB technologies, resulting in relatively large structures. The resulting probes are mainly evaluated on their measurement bandwidth, sensitivity, and spatial resolution. The model-based approach as defined in [1], makes use of signal dependence on the tip-circuit distance in order to differentiate between long-range parasitic contributions to the measurement signal, and short-range local contributions to the measurement signal, which was used to improve the spatial resolution while maintaining sensitivity.

The contactless probing solutions provided in the literature provide a solid foundation for further research. They showcase how a conductive loop can be used to measure both electric and magnetic fields in multicomponent probe designs. Nevertheless, single-component probes have also shown promising characteristics by integrating complex tips, and loops into their design. This research aims to combine 3D-printing technology with thin film technology, in order to integrate a complex loop and tip into a single multicomponent probe. And, to expand the model-based approach so that both contactless RF voltage and current measurements with increased spatial resolution can be performed. The research question covered by this report is therefore formulated as follows:

> **"Can an exchangable probe conduct contactless radio-frequency voltage, and current measurements at a bandwidth of 1 to $26.5\,\mathrm{GHz}$ with micrometre-resolution?"**

Three sub-questions have been formulated which contribute to answering the main research question. The first question addresses how an RF measuring bandwidth can be achieved. From prior research, it was found that the quarter wavelength $\lambda/4$ is an important factor, if the length of the signal path is longer than the quarter wavelength the signal is partially reflected. therefore the signal path needs to be smaller than $\lambda/4$ which corresponds to $c/4\omega$, where c and ω denote the speed of light, and the angular frequency respectively.

The next sub-question addresses the aim for $\mu\mathrm{m}$-spatial resolution. It was found that a miniaturised sensing tip is crucial for a high spatial resolution. Hence, a miniaturised conductive loop and tip are integrated into the design. It should be noted, however, that when miniaturising there is a trade-off between spatial resolution which is increased, and sensitivity, which is decreased. To that end, the model-based approach is utilized, as it differentiates between long-range parasitic, and short-range local contributions to the measurement signal. Local contributions can be isolated with this method, increasing the spatial resolution while the sensitivity is maintained.

In the final sub-question manufacturing techniques are evaluated. A requirement for the probes is that they are replaceable. As the PCBs in this research can be ordered in relatively high quantities, the whole PCB-probe assembly is replaced, simplifying the probe design. To adhere to the bandwidth

requirements the signal path of the probe beyond the waveguide on the PCB should be short $< \lambda/4$. A slope is therefore included which shortens the required probe extension. To improve the spatial resolution a fabrication process resulting in a miniaturised conductive loop and tip is utilized.

In prior research within the research group, 3D-printing techniques have been combined in order to produce structures with similar feature sizes. The presented probe design however addresses an additional challenge. The electrically conductive loop requires a mutually isolated connection between both ends. To realise this a new fabrication process has been developed and patented:"*Skewed Grooves for 3D-Printed Non-Planar Circuits*".

The sub-questions and their answers make up all the pieces of information that are required to answer the main research question. They can hence be combined in one sentence addressing the main research question:

> **"A specialised AFM-probe containing a triangular electrically-conductive loop, with a sharp electrically-conductive tip on top, fabricated through 3D-printing and thermal evaporation, enables contactless RF current and voltage measurements at a bandwidth of 1 to $26.5\,\mathrm{GHz}$ with micrometre-resolution."**

Key Contributions This thesis has touched upon different fields and disciplines. The list of key contributions this research makes is therefore relatively broad. An overview of the identified contributions is listed below:

- **Utilizing 3D-printed probes for near-field scanning applications**
  The literature describes many PCB-fabrication techniques to produce near-field scanning probes. This research however has employed a multiscale 3D-printing process in combination with thermal evaporation to produce near-field scanning probes.
- **Small Tip-circuit distance measurements**
  The probes described in the literature often include some sort of shielding from electric fields. Hence, these probes often conduct measurements at tip-circuit distances of approximately $500\,\mu\mathrm{m}$. The expanded model-based approach eliminates the need for shielding, as the local contributions are mathematically isolated. The multicomponent probe design presented in this research is furthermore compatible with an AFM-setup, allowing it to conduct contactless measurements at tip-circuit distances $z > 100\,\mathrm{nm}$.
- **Expanding the model-based approach [1] to include RF current measurements**
  The model-based measurement approach, as presented in [1], makes use of the dependence of the measurement signal on the tip-circuit distance. It is able to make a distinction between parasitic long-range contributions to the measurement signal, and the local short-range contributions to the measurement signal. In this research, it is expanded to not only conduct contactless RF voltage, but also current, measurements.
- **Incorporating a miniaturised triangular loop shape**
  As PCB-fabrication techniques are often used to fabricate multicomponent near-field probes the dimensions are often limited to approximately $10\,\mu\mathrm{m}$. In this research however, 2PP printing techniques were utilised to produce a triangular conductive loop with a base and height of only $5\,\mu\mathrm{m}$. Next to that, the triangular loop shape lends itself to a higher resolution in combination with the model-based approach, as the signal strength is highest at the apex of the triangle.
- **Producing mutually isolated transmission lines on a single 3D-printed substrate**
  This contribution has even led to a patented technology. A skewed groove is incorporated into the fabricated structure that separates the two signal paths from one another. The beauty of this technique is that it requires only to 3D-print a structure, and then deposit an electrically-conductive film on top through PVD. The result is a structure with only 2 electrical planes, with ohmic isolation between them.

References:

[1] M. Poik, T. Hackl, S. Di Martino, B. M. Berger, S. W. Sattler, and G. Schitter, "A contactless method for measuring amplitude and phase of RF voltages up to 26.5GHz," *IEEE Sensors Journal*, 2024.

5

Recommendations

This research provides a framework for 3D-printed multicomponent near-field scanning probe designs, and model-based contactless RF voltage and current probing. The main goal of this research has been to increase spatial resolution, but as science is about continuous innovation, I have more recommendations on how probe design, but also measurement procedures could be further improved:

- **integrated loop and tip**
  In this research, the conductive loop that enables contactless current measurements is separate from the conductive tip that performs contactless voltage measurements. They can be separately designed and dimensioned in the current setup. However, the resolution that can be achieved is heavily dependent on small tip-circuit distances, a probe design where the conductive loop and tip are integrated into one another, such as in Figure 5.1, enables measurements at even smaller tip-circuit distances.

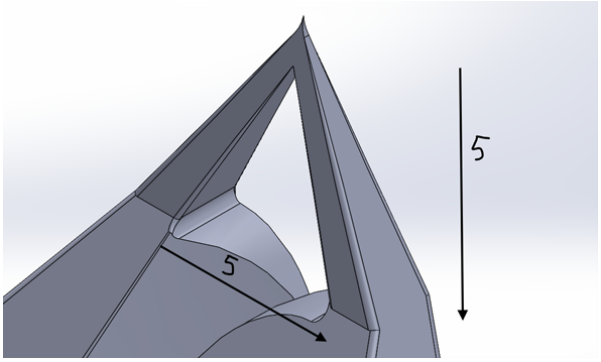

Figure 5.1: Suggestion for an improved probe design with an integrated loop and tip.

- **Experimental Validation of model-based current measurements**
  Due to a lack of time within the project, the model-based approach for contactless RF current measurements is not validated with experiments. In future research, the models can be validated to create a more solid foundation for applications that employ this approach.
- **Reusable clamping solutions**
  In the current probe design, the probe is glued to the PCB to create the PCB-probe assembly. Alternatively, a reusable click-in joint could be included in the 3D-printed probe design, such that the PCB-probe assembly can easily be dismantled so that individual parts can be reused. A concept of such a clamp is shown in Figure 5.2, it has not been further developed in this project as there are other design elements with a higher priority.

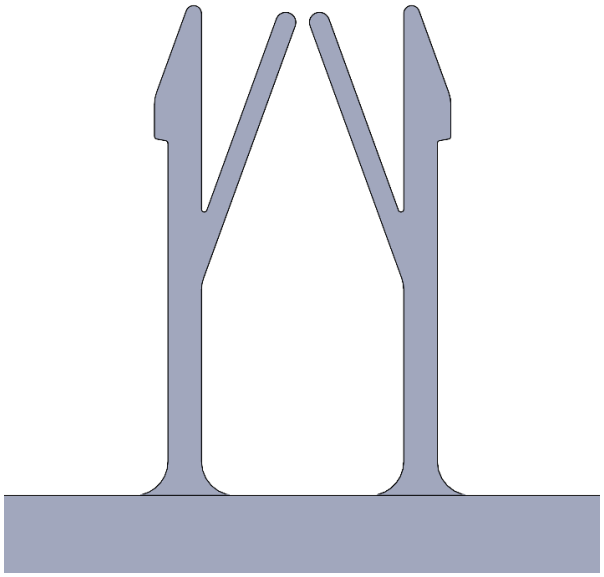

Figure 5.2: A CAD drawing of a suggested clamp for a removable probe.

- **Probe durability improvement**
  It is found that after a few measurements (approximately 75) the tips deform, and need to be replaced. Research into the material properties of the 3D-printed probe can provide valuable insights into how this can be improved. The fabrication parameters during the 2PP process are optimised for a high resolution. They can alternatively be optimised for durability.
- **Tip-circuit positioning procedure**
  The tip-circuit positioning technique as described in the measurement procedure makes use of a tapping AFM-mode. To avoid contact between the tip and circuit altogether, contactless AFM modes can be employed. The probe is perturbed at a certain frequency where either the oscillation amplitude, frequency shift, or phase shift is monitored while the probe is brought in proximity to the surface of the circuit. These are described by for example the Lennard-Jones model [1], which can be used to estimate the tip-circuit distance without making contact between the tip and circuit.
- **Increasing measurement bandwidth by decreasing the probe extension**
  It is found that the measurement bandwidth that can be achieved with the probe is limited by the extension of the probe past the waveguide on the PCB. To decrease this extension a slope was included in the probe design. The length of the cantilever is also extended to increase the reflected laser signal on the photodiode. Further research could optimise these factors to decrease the extension to even further increase the measurement bandwidth.
- **Including waveguides on the probe**
  The current design makes use of straight connections between the probe-PCB interface and the sensing tip. This leads to a mismatch in the impedance, resulting in a partially reflected signal. By including waveguides in the 3D-printed probe design the impedance mismatch can be reduced or even eliminated, to increase the measurement bandwidth.

References:

[1] S.-M. Lin, C.-T. Liauh, W.-R. Wang, and S.-H. Ho, S.-M. Lin, C.-T. Liauh, W.-R. Wang, and S.-H. Ho, “Analytical solutions of the first three frequency shifts of AFM non-uniform probe subjected to the Lennard–Jones force,” *Ultramicroscopy*, vol. 106, no. 6, pp. 508 – 515, Apr. 2006.

6

Reflection

Throughout this thesis and my whole academic career this far, there is one silver lining I always noticed. No matter how much I like to tell myself I don't always have to take the difficult road, I end always end up taking it anyway. Not because I have to of course (nobody forced me to do anything), but because these situations allow me to further develop myself. I started of studying psychology, which was very doable for me as I only spent $14\,\mathrm{h}$ a week on study. But I wanted more challenge, and to learn new things and follow my passion. So I transitioned to mechanical engineering where I had to work A LOT more. Clearly, it was meant to be though, cause I graduated my bachelors cum laude with ease. Here I don't mean it was easy, but the work did not feel like work because I actually wanted to be there. Then during my master, I was determined to NOT graduate cum laude, because I wanted to focus more on developing myself outside of the classroom as well. Evidently, I did not succeed as the courses were just too interesting, especially in my master I felt the opportunity to tailor my courses to my specific area of interest, which again led me to do well. When starting the master thesis I thought to myself, this will be the moment, I will pick an easy subject. But then I came across the RF probing project, and all I saw was the opportunity to work with a university abroad on a topic I had literally NO knowledge of, which would pose a huge challenge disguised as a learning opportunity. I also loved the opportunity to work with micro and nanofabrication techniques as these are not readily available and this might've been my only opportunity.

I had the privilege of not reflecting on this process by myself. I got a scholarship at ASML, where we dived into what drives us, and also how we are motivated. I vividly remember discussing these choices I made with my mentor, Mykyta, and talking about why I made it so hard on myself. The conclusion was clear, by exposing myself to unconvertable and challenging situations, I have the opportunity to attain a lot of new knowledge. Now being at the end of my master's thesis, and likely my academic career this is especially true. Looking back I learned a lot inside of the classroom, but also outside, working with people from different universities, and also seeing the cultural differences. It is an experience I will carry with me for the rest of my life and it motivates me to in difficult situations look back to these lessons, it is all one big learning experience.

A

A Description Of How One Fabricates A Contactless RF Probe

In this appendix, a detailed description of the fabrication process is given. It aims to assist anyone trying to recreate the fabrication process or expand the process to improve its functionality. A multiscale fabrication process is utilised throughout the experiments in this research. Multiscale refers to utilising printers with different resolutions, but also printing speeds. This allows us to maintain the benefits of fast-prototyping, while we can still make use of the high-resolutions that can be achieved with slower printing technologies. To this end, a Digital Light Processing (DLP) stereolithography process is combined with a Two-Photon Polymerisation (2PP) process. The produced structures are inherently not electrically conductive, therefore a metal thin film was deposited through a thermal evaporation process. A flow-chart of the total fabrication process can be found below:

A.1. DLP-Printing

The chip body design is drawn up with `SolidWorks` 3D-CAD software. The resulting part is loaded into `Kudo3D` slicing software compatible with the (Micro2, MicroSLA, USA) DLP-printer. A screenshot of the printing software and setting is provided in Figure A.1. With the dimensions of the design, we are able to fit two chip-bodies on the build-plate. They can hence be printed simultaneously, saving printing time. The step-size of the slope requires a very low layer thickness, whereas the lower bottom section of the chip-body doesn't. Therefore two sections with different layer-thickness are defined.

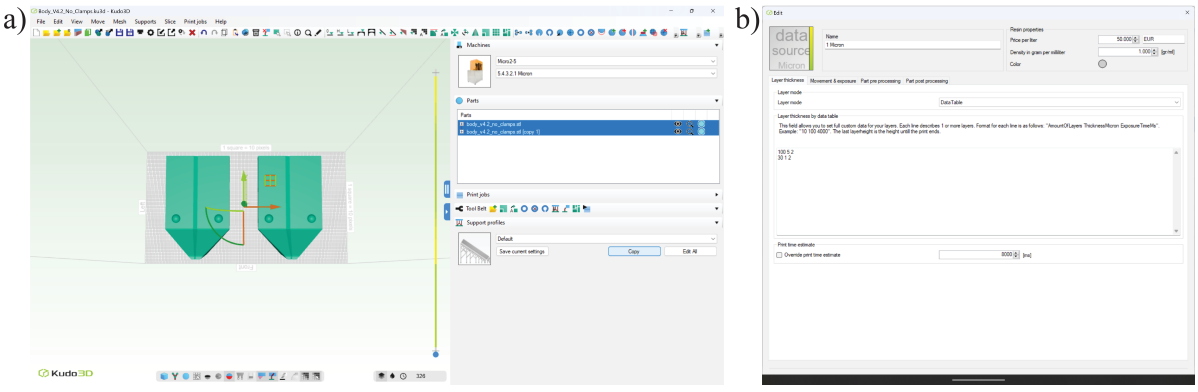

Figure A.1: Screenshots of a) the Kudo3D slicer and b) the slicer thickness settings, for optimised printing speed in the Micro2 DLP printer.

The resin container is filled with (UHR, MicroSLA, USA) photoresist. the printer can be controlled through a wireless local connection. Through this interface, the recipe files produced by the slicer are

uploaded. The build plate is lowered into the container, and thereafter the printing process can be started.

When the printing is finished, the build plate can be removed including the chip-bodies. They are cleaned together as an assembly for $2\,\mathrm{min}$ in a first IPA-solution, and $2\,\mathrm{min}$ in a second IPA-solution. After a certain amount of uses, the IPA-solution is polluted, which can visually be detected by a colour change. In that case, the first rinsing solution is discarded, and replaced by the second solution. The second solution is refiled with a new fresh IPA-solution.

After cleaning a scalpel is used to remove the chip-bodies from the build plate. It often occurred that during removal, a lip was formed beside the bottom of the chip body, as depicted in Figure A.2a. After the thermal evaporation process, this could lead to a short. Two countermeasures are taken to remedy this issue. As can be seen in Figure A.2b, a notch with an angle of $45°$ is included in the design at the bottom of the chip-body. Next to that, any remaining lips are removed after the printing process with a scalpel. To be honest, this does require a certain skill-level, as the chip-bodies are very small, and have to be held with a tweezer during this removal process.

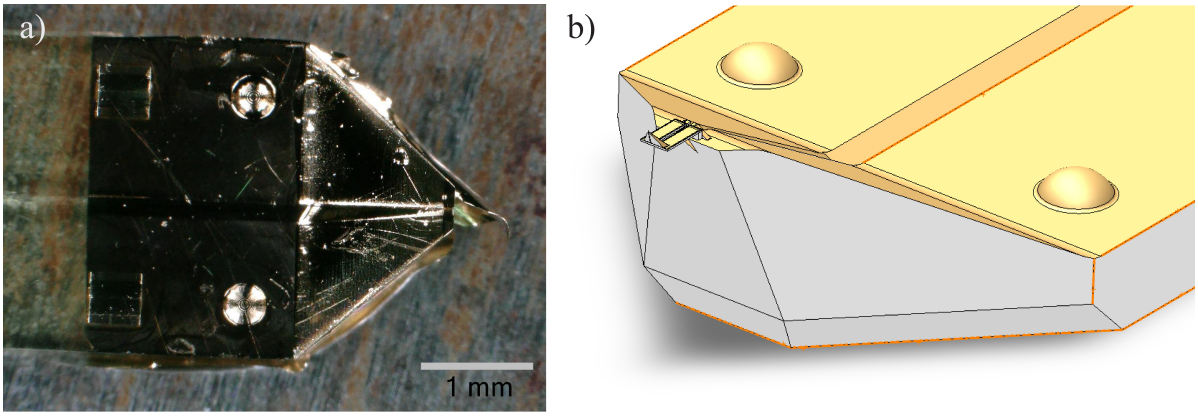

Figure A.2: In a) the effect of thermally evaporating a chip-body without removing lips can be seen. In b) this is remedied by including a notch.

After the DLP-printing process, the chip-bodies are optically evaluated for any deficits with the microscope in the cleanroom. The chip-bodies required no further preparation prior to the 2PP-process.

A.1.1. Custom Sample Holder

The sample 9x9 sample holders that are compatible with the 2PP-setup (Photonic Professional GT Laser Lithography System, Nanoscribe GmbH, Germany) are not inherently suitable for mounting the chip bodies. A custom chip-body holder is therefore printed with a DLP-printer (Micro Plus HiRes, EnvisionTEC GmbH, Germany), it is depicted in Figure A.3. This printer has a larger build-platform compared to the DLP printer used to manufacture the chip-bodies.

The chip-body holder contains overhanging structures that are printed with supports. After the printing process the structure is developed in an IPA solution for $20\,\mathrm{min}$. Subsequentially, it is clamped between two microscope slides that are taped together to avoid warping of the overhanging structures, and post-exposure cured in a UV-oven at $80\,°\mathrm{C}$ for another $20\,\mathrm{min}$. The final step is to remove the supports, which become brittle due to the post-exposure curing process, making them easier to remove while keeping the overhanging elements.

It is experimentally determined that an interface can be found more easily when a substrate with a high reflectivity is used. Therefore a reflective coating is applied to the chip-body holder in the final fabrication step. A thermal evaporator (Temescal FC-2000, Ferrotec USA, USA) is used to first deposit a $10\,\mathrm{nm}$ thick thin film of titanium (Ti), and subsequentially a $100\,\mathrm{nm}$ thick thin film of gold (Au). It is deposited according to the same recipe as the thin film deposition process discussed in .

X

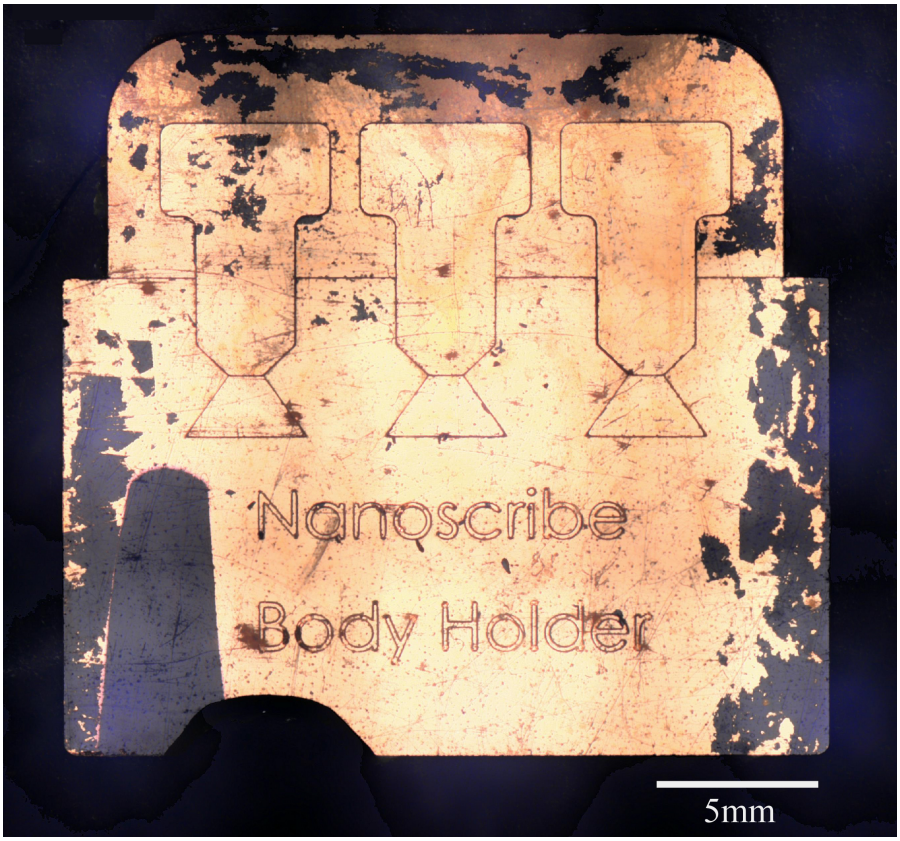

Figure A.3: Picture of the chip-body holder.

A.2. 2PP-Printing

Using tweezers, the chip bodies are mounted into the chip-body holder. They are first taped down so that they stay in place. A drop of resin is subsequentially deposited on the printing areas. The chip-body holder is then mounted into the 9x9 sample holder where it is also taped down. This process is visualised in Figure A.4.

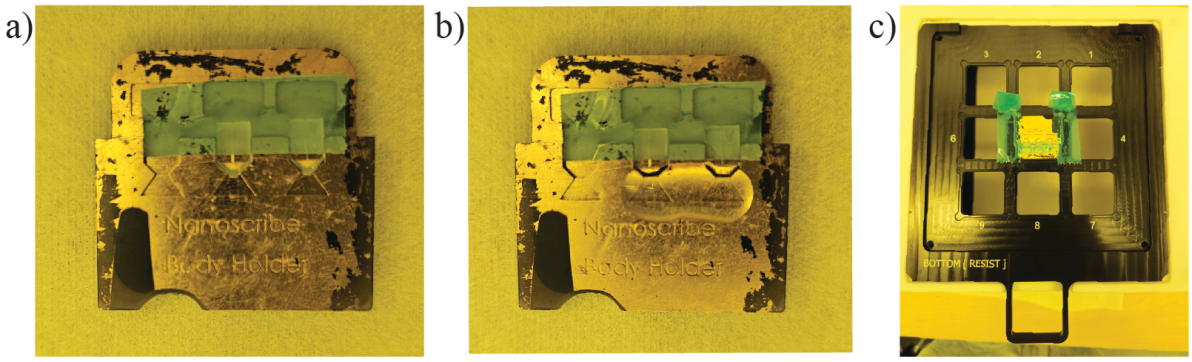

Figure A.4: Pictures of the loading procedure, where a) the chip bodies are loaded into the chip-body holder, and b) a drop of photoresist is deposited in the printing area, and c) the chip-body holder is transferred to the sample holder.

The 2PP-setup is first configured with a 63x magnifying objective, equipped with a felt ring. Afterwards, the 9x9 sample holder is mounted into the setup. When the `Describe` slicing software was opened, an `.stl` file could be opened to generate a `.gwl`, and `.job` file. The `.job` file is used to execute the printing, whereas the `.gwl` file contains all the geometrical information and printing settings. A `.job` file can be modified to include multiple `.gwl` files to create complex structures with different settings for distinct geometries. A screenshot of the `.job` file used in this printing process is depicted in Figure A.5.

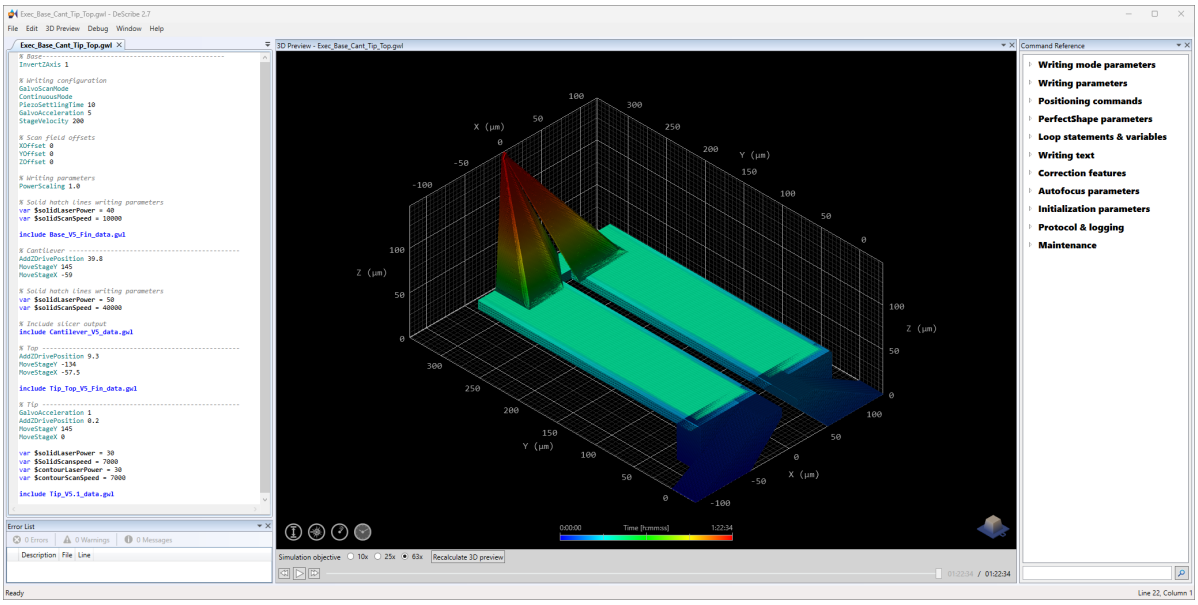

Figure A.5: A screenshot of the `Describe` interface.

Finding the optimal printing parameters is an iterative process. The optimal parameters can vary with different setups and environments. For this research, they are optimised to the point where they yield stable structures with a sufficient resolution for the application. A list of the printer settings can be found in Table A.1. Next to these settings, the avoid flying blocks command is unchecked. If left checked it can lead to errors when the interface is manually identified. The find interface command is also removed as it is manually identified.

The cantilever is furthermore printed with blocks that have a shear angle of $45°$. The block size is set

to $8\,\mu\mathrm{m}$ with an overlap of $4\,\mu\mathrm{m}$. Furthermore, the hatchlines are written in alternate directions.

Table A.1: Printing parameters used in the 2PP process.

	Base	Cantilever	Sensing Tip
Laser power*	$40\,\%$	$50\,\%$	$30\,\%$
Scanning speed ($\mathrm{mm\,s^{-1}}$)	10	40	7
Slicing distance (µm)	0.3	0.2	0.1
Hatching distance (µm)	0.3	0.2	0.1
Galvo acceleration ($\mathrm{V\,ms^{-2}}$)	5	5	1

* Given as the percentage of the total laser power of $50\,\mathrm{mW}$

When the samples are inserted into the 2PP-setup, and the job files are loaded, the operating system (`NanoWrite`) is started. It is already mentioned but the interface is manually identified, to ensure bonding between the DLP and 2PP part the printing process is started approximately $5\,\mu\mathrm{m}$ below the DLP interface. It is known that when the system is initiated the XY-coordinate system is reset. Therefore the chip-body holder has been designed such that when the stage is objective approaches the sample in the initial XY-coordinates, markers can be identified. A screenshot of what that looks like is depicted in Figure A.6a. When the interface is found first a dot is printed to find the origin of the printer coordinate system. This location is marked with the internal coordinate system. It is then aligned to a reference point (In our case the edge of the skewed-groove). The printing process is then started and the structure will automatically be printed, such as can be seen in Figure A.6b.

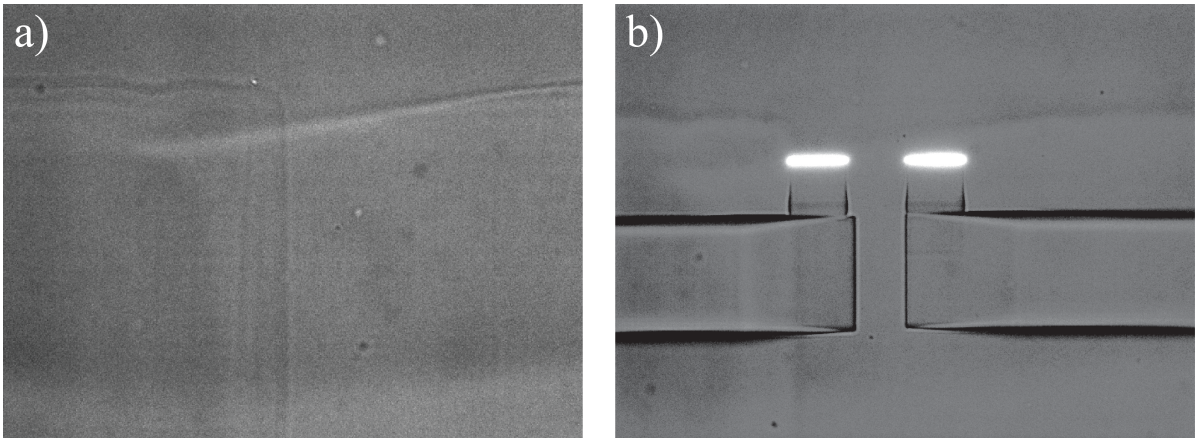

Figure A.6: Screenshots of the positioning procedure with a) what can be seen when the interface needs to be found, and b) what it looks like during the printing process.

When the printing process is complete the samples are removed from the 2PP-setup. The chip-body holders including the probes are removed and developed in two steps. They are first developed for $5\,\mathrm{min}$ in a PGMEA-solution. In the second development step, they are developed for another $20\,\mathrm{min}$ in an IPA-solution. The probes are removed from the chip-body holder, which is now clean and ready to be used again. As in our lab-setup there was no thermal evaporator available, the probes were loaded in gel-packs so that they could be moved to a different lab.

A.3. Thermal Evaporation

The last step in the fabrication process is thermal evaporation. The samples are taken into the lab containing the thermal evaporator (Temescal FC-2000, Ferrotec USA, USA). The samples are loaded onto the sample holder as depicted in Figure A.7. Clamps with low clamping force are used to secure the probes. A picture is taken, and numbers are assigned to track the probes throughout the process. The sample holder is then mounted in the process chamber and the lid is closed. The next step is to evacuate the system to a low pressure prior to starting the deposition recipe.

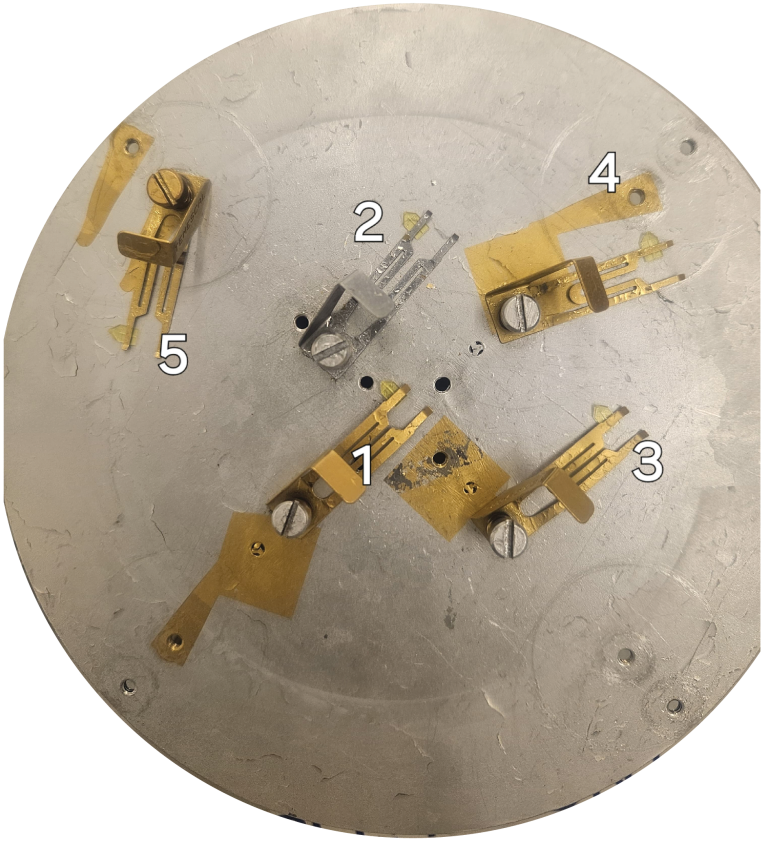

Figure A.7: Picture of probes loaded into the thermal evaporator sample holder, including numbers and clamp orientation for tracking individual probes.

In the first deposition step a Titanium (Ti) thin film of $10\,\mathrm{nm}$ is deposited. When a pressure of $2\,\mathrm{mTorr}$ is achieved, an electron gun starts heating the material. When the material is heated to a set temperature, the deposition rate should be constant. While the sample holder is rotating with $10\,\mathrm{RPM}$, a shutter is removed and the evaporation process starts. A deposition rate of $0.5\,\mathrm{Å\,s^{-1}}$ is selected. There however is always a slight deviation between the initial deposition rate, and the rate that is selected in the recipe, the system automatically corrects the electron beam to achieve the proper deposition rate.

The second deposition step can be initiated directly after the first deposition. In the second step, Gold (Au) is deposited at a rate of $1.0\,\mathrm{Å\,s^{-1}}$, to reach a final thickness of $100\,\mathrm{nm}$. The sample holder is again rotated with a speed of $10\,\mathrm{RPM}$, and the pressure threshold to start the deposition process is set to $3\,\mathrm{mTorr}$. Throughout the deposition process, the substrate temperature is carefully monitored. With the described recipe it stays below $60\,^{\circ}\mathrm{C}$.

After the deposition process is complete the process chamber is vented, and the lid can be removed to access the sample holder. The probes are carefully transferred to a gell-pack, and put into an Electrostatic Discharge (ESD)-safe bag. It is found that this is an important step, as we are dealing with ESD-sensitive devices. In ideal circumstances, a grounding wristband is used when handling the devices. Also, clothing that generates less static electricity can prevent ESD effects.

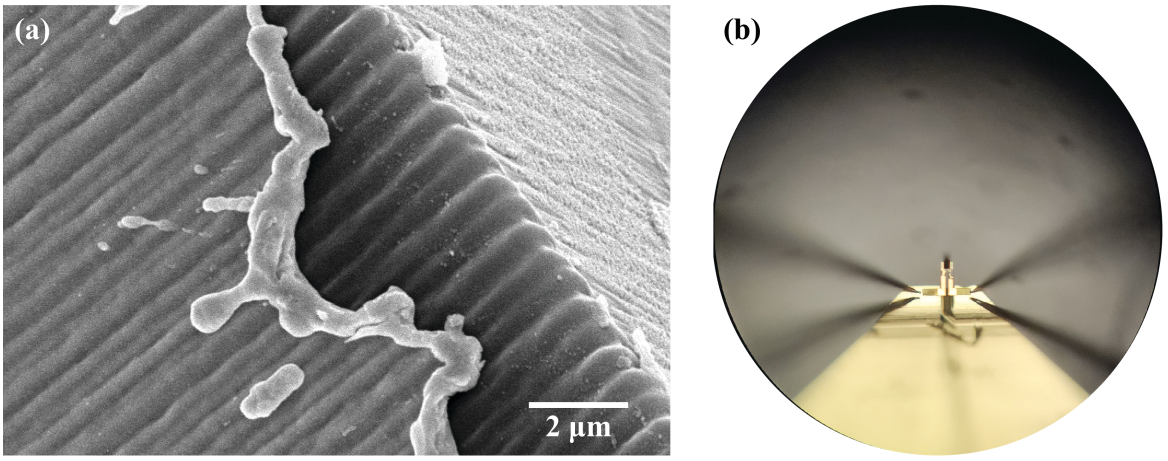

Figure A.8: The effects of ESD visualised in a) SEM-images, and b) in a 4-point probe.

To make sure there is an electrical connection, and the thermal evaporation process is successfully executed, a 4-point probe is used and SEM images are taken. It can be seen from Figure A.8a, what the effects of ESD look like through a microscope. When the 4-point probe is connected, the instantaneous current flow is so high that the electrically conductive film is destroyed, as depicted in Figure A.8b. It can therefore be concluded that ESD effects need to be considered when handling these devices, to mitigate a charge buildup in the thin film.

A.4. Extra Reference Material

In this section, extra pictures for reference are incorporated. Such a fabrication process is definitely not straightforward, and some of the additional hurdles I encountered are discussed in this chapter.

Thermal Evaporation During this process, it is possible to run out of material. Therefore a viewing window is installed in the thermal evaporator. In Figure A.9, a picture can be seen that is taken through this window. When the deposition material droplet becomes too small, the electron beam will not only heat up the deposition material, but also the socket itself. This can lead to impure material deposition. It is therefore important to monitor the droplet size, and make sure the deposition material is replenished before it becomes too small.

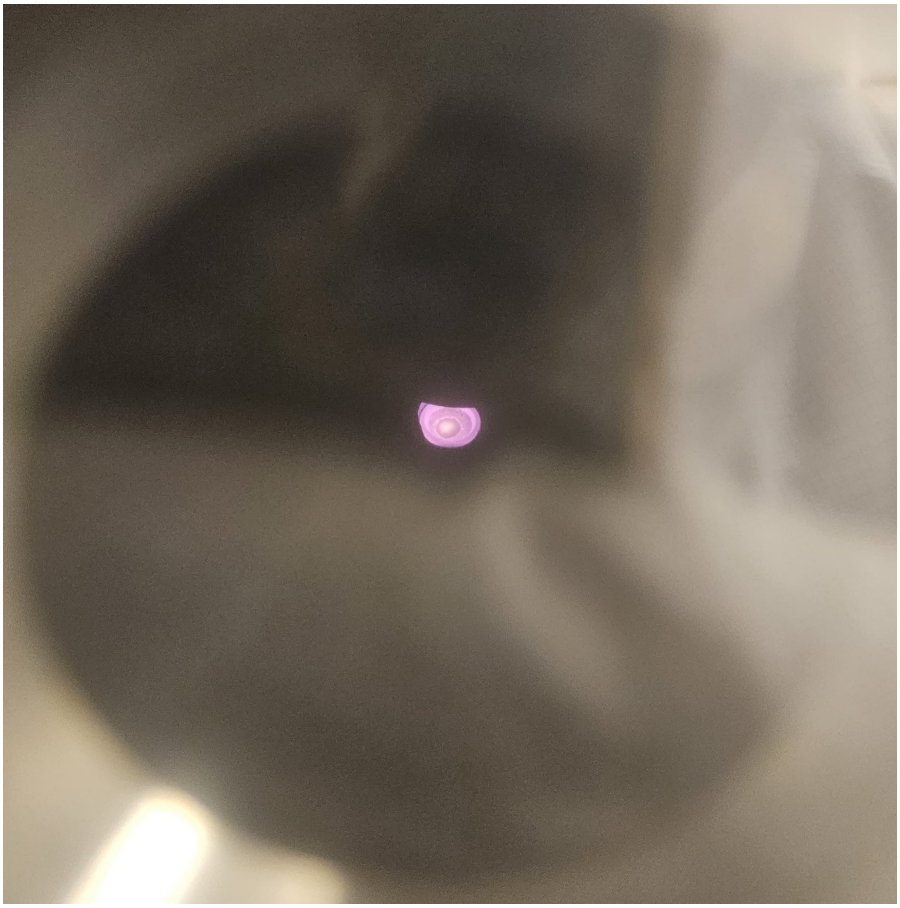

Figure A.9: Picture of the socket during the evaporation process, when taking a close look, one can see the drop of material that is being deposited.

Tip Optimisation The optimisation process of 2PP-printed parts is an iterative process. In Figure A.10c for example, a tip from a 'dose test' is photographed. In this test, a grid is printed of only the top $20\,\mu\mathrm{m}$ of the tip with varying laser power and scanning speed. SEM images are then taken of every tip to determine the printing settings that yield the best results, which can be found in Table A.1. The bonding between the DLP and 2PP print is also investigated, by initialising the 2PP printing process approximately $5\,\mu\mathrm{m}$ below the chip-body interface, the structures have sufficient support.

To make sure the design made in `SolidWorks` translates to the desired structures, multiple of these tests are executed, also with different parameters such as slicing, and hatching distance. When all the parameters are optimised, the design elements are put together, forming the complete probe as depicted in Figure A.10, which shows the previous probe design with a relatively small cantilever. It is found that due to the small cantilever, not enough of the laser signal can be read out by the photodiode. Therefore, the final design features a much wider, and longer cantilever, which remedies this issue.

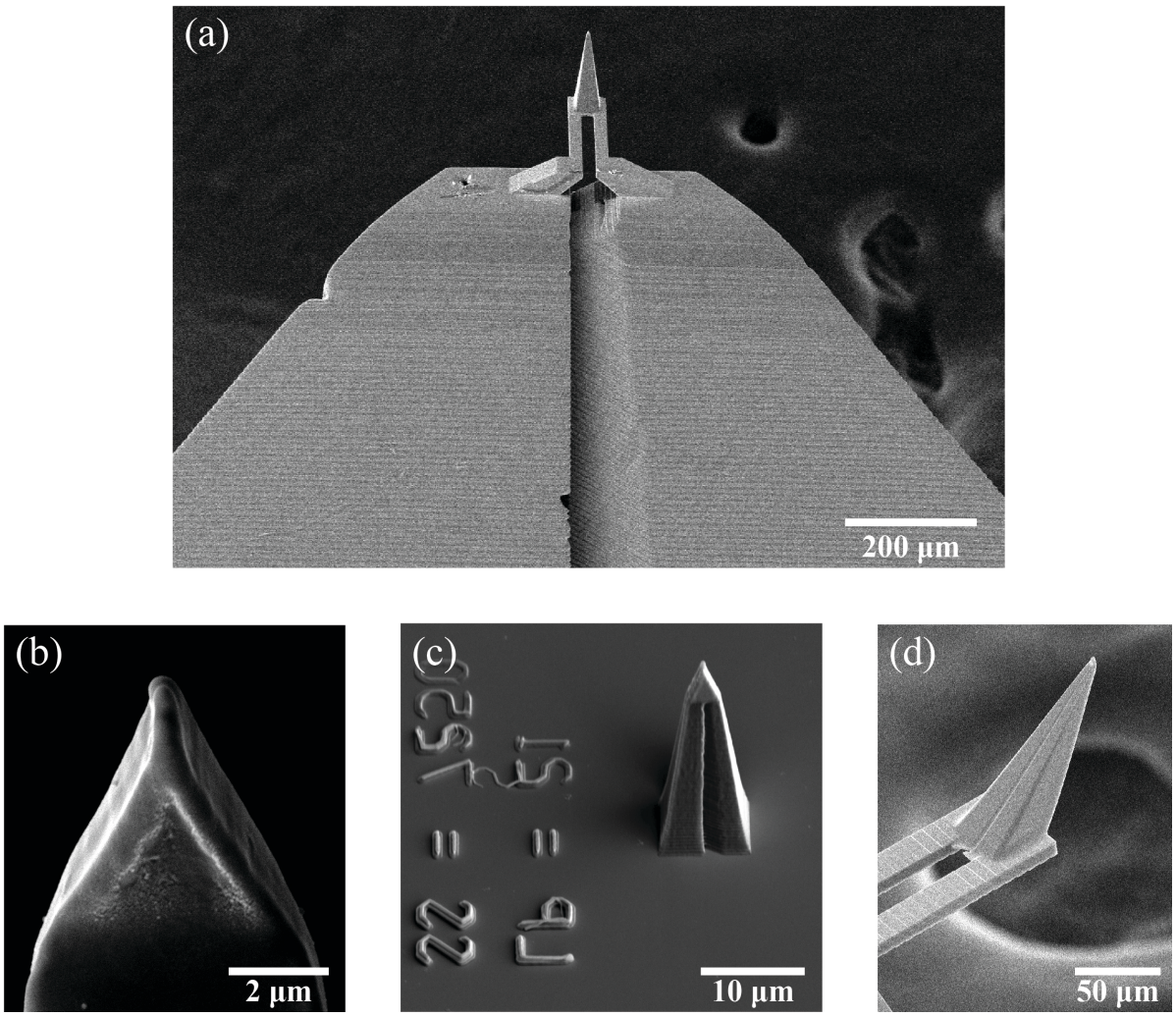

Figure A.10: SEM-images that were taken during the optimisation process of the printing parameters with a) the final result, b) an inspection of the tip apex, c) inspection of the last $20\,\mu\mathrm{m}$ of the tip, and d) inspection of the cantilever and tip together.

Cantilever The cantilever is fabricated with increments. This is realised by defining blocks in the slicing software that have an overlap with the previously printed block. As can be seen in Figure A.11, overhanging structures can successfully be printed this way, but it does lead to increased surface roughness. In later probe designs, this was overcome by adding an additional layer on top of the cantilever after it was fully printed.

The probe cantilevers are inspected with an optical microscope and an SEM. They can characterise the sagging of the cantilever. Therefore not only pictures have been taken from above, but also at an angle as seen in Figure A.11a, and Figure A.11c.

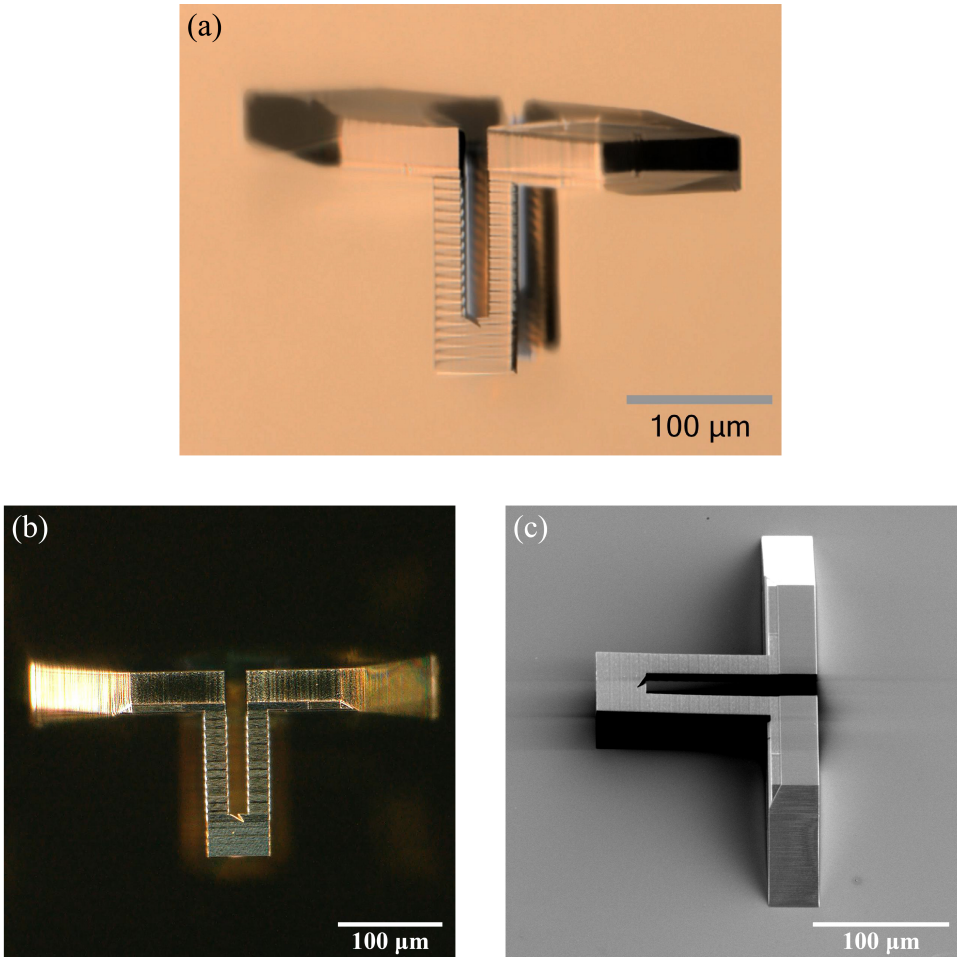

Figure A.11: Pictures of the fabricated overhanging cantilever a) an optical image of the cantilever at an angle of $30°$, b) another optical image of the cantilever taken from above, and c) an SEM image of the cantilever at an angle of $37.5°$.

Packaging The probes are checked one final time before they are sent of to Vienna, where they are tested, and measurements are taken with them. Transparent ESD-safe bags and gell-packs are employed. The probes can therefore be inspected with the optical microscope without taking them out of the packaging.

A photograph was also taken prior to the thermal evaporation process to track any defects in the probes. Such a picture can be seen in Figure A.12. The probe was checked overall, and pictures with an increasing zoom were taken to make sure there were also no defects (that can optically be identified) in the cantilever, and tip.

A photograph showing the final check is depicted in Figure A.13. It can be seen that the tip did not break off, or got removed during the thermal evaporation process. It can also be seen that there is a separation along the middle of the entire probe.

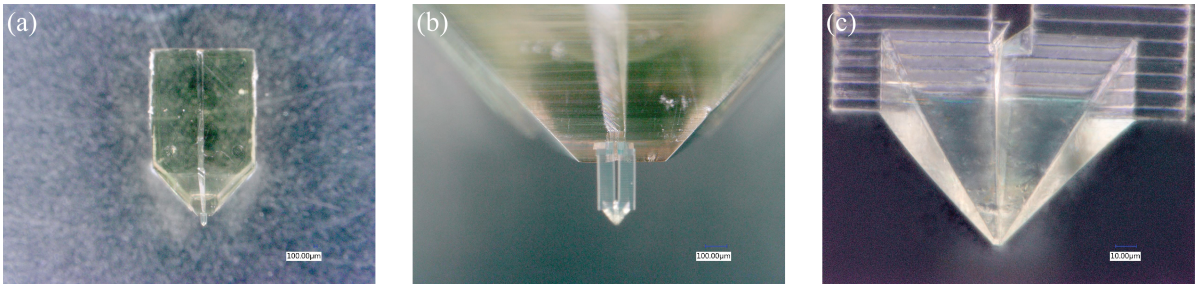

Figure A.12: Optical inspection of the probe prior to thermal evaporation of a) the whole probe, b) the cantilever, and c) the tip.

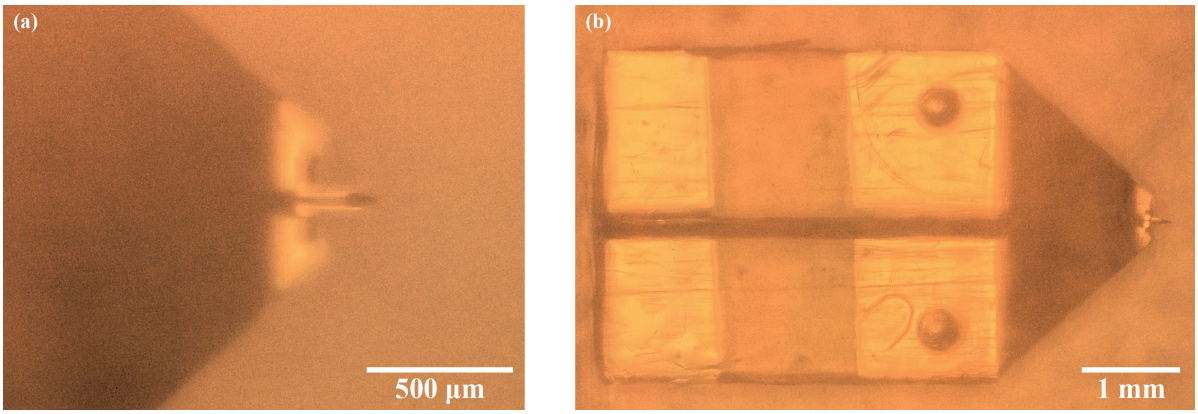

Figure A.13: Optical microscopy images taken through an ESD-safe bag, and gel-pack. Where a) shows a zoom-in of the tip, and b) shows the overall probe.

B

Calculations and models

In this section of the report, the calculations and mathematical models are given that were used throughout the report.

B.1. Impedance of the loop.

It was mentioned in the paper, that the impedance of the loop needs to be small, compared to the characteristic impedance of the transmission line, for the assumption of the model-based RF current measurements to hold. The loop impedance (Z_{loop}) can be subdivided into a contribution from the resistance (R_{loop}), and a contribution from the inductance (L_{loop}).

To calculate the resistance (R_{loop}), the length of the thin film deposited on the loop is important. First the cross-sectional area (A_{cross}) of the deposited film is calculated as:

$$A_{\text{cross}} = \text{width} \cdot \text{thickness} = 2\,\mu\text{m} \cdot 110\,\text{nm} = 0.22\,\mu\text{m}^2 \tag{B.1}$$

Second, the length of the thin film (l_{loop}) that forms the electrically conductive loop is calculated as:

$$l_{\text{loop}} = 2\sqrt{\left(\frac{\text{base}}{2}\right)^2 + (\text{height})^2} = 2\sqrt{\left(\frac{5\,\mu\text{m}}{2}\right)^2 + (5\,\mu\text{m})^2} = 11.18\,\mu\text{m} \tag{B.2}$$

The Equation B.1, and B.2 can now be combined with the resistivity of gold, which is a material property, to find the resistance across the loop as follows:

$$R_{\text{loop}} = \rho\frac{l_{\text{loop}}}{A_{\text{cross}}} = 0.0244\,\mu\text{m}\,\Omega\frac{11.18\,\mu\text{m}}{0.22\,\mu\text{m}^2} = 1.24\,\Omega \tag{B.3}$$

Next to that, the inductance of the loop (L_{loop}) also needs to be calculated in order to find the proper impedance of the loop. For this the area enclosed by the loop, as well as the perimeter of the enclosed area.

The area enclosed by the loop(A_{loop}) can be calculated as:

$$A_{\text{loop}} = \frac{1}{2} \cdot \text{base} \cdot \text{height} = \frac{1}{2} \cdot 5\,\mu\text{m} \cdot 5\,\mu\text{m} = 12.5\,\mu\text{m}^2 \tag{B.4}$$

The perimeter around the loop (l_{per}) also includes the underside, and can hence be calculated as:

$$l_{\text{per}} = l_{\text{loop}} + \text{base} = 11.18\,\mu\text{m} + 5\,\mu\text{m} = 16.18\,\mu\text{m} \tag{B.5}$$

The inductance in the loop (L_{loop}) can now be calculated using Equation B.4, and B.5 to find the following:

$$L_{\text{loop}} = \mu_0 \mu_r \frac{A_{\text{loop}}}{l_{\text{per}}} = 1.25 \times 10^{-6}\,\mathrm{H\,m^{-1}} 1.8 \frac{12.5\,\mu\mathrm{m}^2}{16.18\,\mu\mathrm{m}} = 1.74\,\mathrm{pH} \tag{B.6}$$

The total impedance in the loop (Z_{l}) is then given by:

$$Z_{\text{l}} = R_{\text{loop}} + j\omega L_{\text{loop}} \tag{B.7}$$

The maximum frequency considered is equal to $26.5\,\mathrm{GHz}$. The maximum value of the loop impedance is therefore approximately $1.29\,\Omega$. As this value is way below the characteristic impedance of the transmission lines (Z_0 = $50\,\Omega$), the assumption holds, and the model-based approach should be valid across the entire frequency range.

B.2. MATLAB code for EMF-simulation

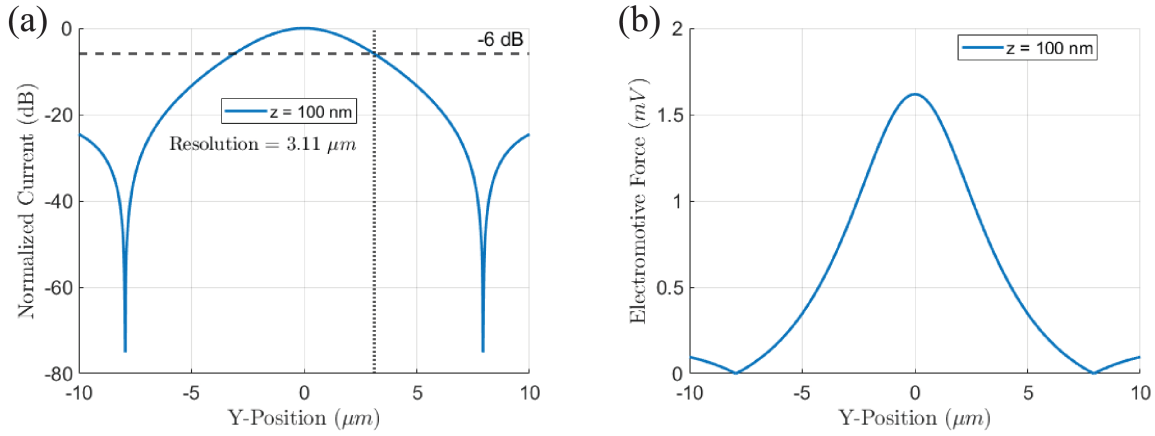

Figure B.1: Plot results of the analytical MATLAB simulations with a) the normalised plot, used to calculate the spatial resolution, and b) the linear plot, showing the EMF induced over the loop and the amplitude of the expected signal.

A MATLAB code is written that can be used to simulate the Electromotive Force (EMF) that is induced over an electrically conductive loop as a result of a current on the DUT. The code produces two graphs, as depicted in Figure B.1. One of these plots is used to determine the spatial resolution, whereas the other is used to determine the sensitivity of the probe to RF currents. The code that was used to create these plots is given below:

```
% Clear workspace and define symbolic variables
clear all
syms y z y_2 y_t

% Input Current Parameters
I_val = 10e-6;          % Input Current Amplitude (A)
omega = 1e9;            % Frequency of Input Current (Hz)
w_s = 2e-6;             % Microstrip Width (m)

% Current Distribution Along the Microstrip
Is = @(y_2) (1 + abs(2 * y_2 / w_s).^3) .* (abs(y_2) <= w_s / 2);

% Normalize the Current Distribution
normalization_factor = integral(@(y_2) Is(y_2), -w_s / 2, w_s / 2);
Is_func = @(y_2) I_val * Is(y_2) / normalization_factor;

% Magnetic Permeability in Vacuum
mu = 1.25663706e-6;

% Geometrical Variables
d = 5e-6;               % Ground-plane to conductor distance (m)
t = 2e-6;               % Passivation layer thickness (m)

% Loop Dimensions
xe = 5e-6;              % Width of the loop at the top (m)
z0_values = t + 100e-9; % Tip-sample distances (m)
ze_values = z0_values + 5e-6; % Height of the tip (m)
y_vals = linspace(-10e-6, 10e-6, 1000); % Y-coordinates for measurement
loop_thickness = 2e-6;  % Loop thickness in y-direction (m)

% Transmission Line Dimensions
x_tr = 10e-9;           % Transmission line width (m)
ze_tr = z0_values + 100e-6; % Tip height (m)

% Initialize Results Storage
flux_Loop = zeros(length(z0_values), length(y_vals));
flux = zeros(length(z0_values), length(y_vals));
EMF = zeros(length(z0_values), length(y_vals));
EMF_n = zeros(length(z0_values), length(y_vals));

```

```
% Tip Geometry
a = xe ./ (ze_values - z0_values);
b = -a .* z0_values;

% Compute Magnetic Field for Each z0
for j = 1:length(z0_values)
    z0 = z0_values(j);
    ze = ze_values(j);

    for i = 1:numel(y_vals)
        y_val = y_vals(i);
        flux_sum = 0;
        num_points = 50; % Number of points for thickness summation
        step = loop_thickness / num_points;

        for k = 1:(num_points+1)
            y_t = y_val - loop_thickness / 2 + (k-1) * step;

            % Magnetic Field Integrands
            Bn1_integrand = @(y_2, z_val) ...
                (mu / (2 * pi)) * Is_func(y_2) .* (z_val ./ ((y_t - y_2).^2 + z_val.^2));
            Bn2_integrand = @(y_2, z_val) ...
                (mu / (2 * pi)) * Is_func(y_2) .* ((z_val + 2 * d) ./ ((y_t - y_2).^2 + (
                    z_val + 2 * d).^2));

            % Perform Double Integration
            flux_sum = flux_sum + integral2(@(y_2, z_val) ...
                (Bn1_integrand(y_2, z_val) - Bn2_integrand(y_2, z_val)), ...
                -w_s / 2, w_s / 2, z0, ze);
        end

        % Average Flux and Compute EMF
        flux_Loop(j, i) = flux_sum / (num_points + 1);
        flux(j, i) = abs(flux_Loop(j, i));
        EMF(j, i) = flux(j, i) * omega;
    end

    % Normalize EMF
    max_temp = max(EMF(j, :));
    EMF_n(j, :) = db(EMF(j, :) ./ max_temp);
end

% Plot 1: Non-Normalized EMF
figure(1);
clf;
hold on;
for j = 1:length(z0_values)
    plot(y_vals * 1e6, EMF(j, :) * 1e6, 'LineWidth', 2, ...
        'DisplayName', ['z = ', num2str(z0_values(j) * 1e9), ' nm']);
end
hold off;
grid on;
xlabel('y ($\mu m$)', 'FontSize', 14, 'Interpreter', 'latex');
ylabel('Electromotive Force ($\mu V$)', 'FontSize', 14, 'Interpreter', 'latex');
xlim([min(y_vals) * 1e6 max(y_vals) * 1e6]);
legend('Location', 'best');
set(gca, 'FontSize', 14);

% Plot 2: Normalized EMF
figure(2);
clf;
hold on;
for j = 1:length(z0_values)
    plot(y_vals * 1e6, EMF_n(j, :), 'LineWidth', 2, ...
        'DisplayName', ['z = ', num2str((z0_values(j) - t) * 1e9), ' nm']);

    % Mark Resolution at -6 dB
    intersection_idx = find(EMF_n(j, :) >= -6, 1, 'last');
    if ~isempty(intersection_idx)
        intersection_x = y_vals(intersection_idx) * 1e6;
        xline(intersection_x, ':k', 'LineWidth', 2, 'HandleVisibility', 'off');
```

```
        text(intersection_x - 0.8, -30, ...
            ['Resolution = ', num2str(intersection_x + w_s / 2, '%.2f'), ' $\mu m$'], ...
            'HorizontalAlignment', 'right', 'FontSize', 14, 'Interpreter', 'latex');
    end
end
hold off;
grid on;
yline(-6, '--k', '-6 dB', 'LineWidth', 2, 'HandleVisibility', 'off');
xlabel('Y-Position ($\mu m$)', 'FontSize', 14, 'Interpreter', 'latex');
ylabel('Normalized Current (dB)', 'FontSize', 14, 'Interpreter', 'latex');
xlim([min(y_vals) * 1e6 max(y_vals) * 1e6]);
legend('Location', 'best', 'FontSize', 12);
set(gca, 'FontSize', 14);
```